

The MUSE Hubble Ultra Deep Field Survey. X. Lyα equivalent widths at $2.9 < z < 6.6$

T. Hashimoto, T. Garel, B. Guiderdoni, A. B. Drake, R. Bacon, J. Blaizot, J. Richard, F. Leclercq, H. Inami, A. Verhamme, et al.

▶ **To cite this version:**

T. Hashimoto, T. Garel, B. Guiderdoni, A. B. Drake, R. Bacon, et al.. The MUSE Hubble Ultra Deep Field Survey. X. Lyα equivalent widths at $2.9 < z < 6.6$. Astronomy and Astrophysics - A&A, 2017, 608, 10.1051/0004-6361/201731579 . insu-03710606

HAL Id: insu-03710606
https://insu.hal.science/insu-03710606

Submitted on 1 Jul 2022

HAL is a multi-disciplinary open access archive for the deposit and dissemination of scientific research documents, whether they are published or not. The documents may come from teaching and research institutions in France or abroad, or from public or private research centers.

L'archive ouverte pluridisciplinaire **HAL**, est destinée au dépôt et à la diffusion de documents scientifiques de niveau recherche, publiés ou non, émanant des établissements d'enseignement et de recherche français ou étrangers, des laboratoires publics ou privés.

A&A 608, A10 (2017)
DOI: 10.1051/0004-6361/201731579
© ESO 2017

Astronomy & Astrophysics
Special issue

The MUSE Hubble Ultra Deep Field Survey

The MUSE *Hubble* Ultra Deep Field Survey

X. Lyα equivalent widths at 2.9 < z < 6.6

T. Hashimoto[1,2,3,4], T. Garel[1], B. Guiderdoni[1], A. B. Drake[1], R. Bacon[1], J. Blaizot[1], J. Richard[1], F. Leclercq[1], H. Inami[1], A. Verhamme[1,5], R. Bouwens[6], J. Brinchmann[6,7], S. Cantalupo[8], M. Carollo[8], J. Caruana[9,10], E. C. Herenz[11], J. Kerutt[12], R. A. Marino[8], P. Mitchell[1], and J. Schaye[6]

[1] Univ. Lyon, Univ. Lyon1, ENS de Lyon, CNRS, Centre de Recherche Astrophysique de Lyon, UMR 5574, 69230 Saint-Genis-Laval, France
[2] Department of Astronomy, Graduate School of Science, The University of Tokyo, 113-0033 Tokyo, Japan
[3] National Astronomical Observatory of Japan, 2-21-1 Osawa, Mitaka, 181-8588 Tokyo, Japan
[4] College of General Education, Osaka Sangyo University, 3-1-1 Nakagaito, Daito, 574-8530 Osaka, Japan
e-mail: thashimoto@est.osaka-sandai.ac.jp
[5] Observatoire de Genève, Université de Genève, 51 Ch. des Maillettes, 1290 Versoix, Switzerland
[6] Leiden Observatory, PO Box 9513, 2300 RA Leiden, The Netherlands
[7] Instituto de Astrofísica e Ciências do Espaço, Universidade do Porto, CAUP, rua das Estrelas, 4150-762 Porto, Portugal
[8] Institute for Astronomy, Department of Physics, ETH Zürich, Wolfgang, Pauli, Strasse 27, 8093 Zürich, Switzerland
[9] Department of Physics, University of Malta, Msida MSD 2080, Malta
[10] Institute for Space Sciences & Astronomy, University of Malta, Msida MSD 2080, Malta
[11] Department of Astronomy, Stockholm University, AlbaNova University Centre, 106 91 Stockholm, Sweden
[12] Leibniz-Institut für Astrophysik Potsdam (AIP), An der Sternwarte 16, 14482 Potsdam, Germany

Received 17 July 2017 / Accepted 21 October 2017

ABSTRACT

We present rest-frame Lyα equivalent widths (EW_0) of 417 Lyα emitters (LAEs) detected with Multi Unit Spectroscopic Explorer (MUSE) on the Very Large Telescope (VLT) at $2.9 < z < 6.6$ in the *Hubble* Ultra Deep Field. Based on the deep MUSE spectroscopy and ancillary *Hubble* Space Telescope (HST) photometry data, we carefully measured EW_0 values taking into account extended Lyα emission and UV continuum slopes (β). Our LAEs reach unprecedented depths, both in Lyα luminosities and UV absolute magnitudes, from $\log(L_{\mathrm{Ly}\alpha}/\mathrm{erg\ s^{-1}}) \sim 41.0$ to 43.0 and from $M_{\mathrm{UV}} \sim -16$ to -21 ($0.01-1.0\ L^*_{z=3}$). The EW_0 values span the range of ~5 to 240 Å or larger, and their distribution can be well fitted by an exponential law $N = N_0 \exp(-EW_0/w_0)$. Owing to the high dynamic range in M_{UV}, we find that the scale factor, w_0, depends on M_{UV} in the sense that including fainter M_{UV} objects increases w_0, i.e., the Ando effect. The results indicate that selection functions affect the EW_0 scale factor. Taking these effects into account, we find that our w_0 values are consistent with those in the literature within 1σ uncertainties at $2.9 < z < 6.6$ at a given threshold of M_{UV} and $L_{\mathrm{Ly}\alpha}$. Interestingly, we find 12 objects with $EW_0 > 200$ Å above 1σ uncertainties. Two of these 12 LAEs show signatures of merger or AGN activity: the weak CIV λ1549 emission line. For the remaining 10 very large EW_0 LAEs, we find that the EW_0 values can be reproduced by young stellar ages (<100 Myr) and low metallicities ($\lesssim 0.02\ Z_\odot$). Otherwise, at least part of the Lyα emission in these LAEs needs to arise from anisotropic radiative transfer effects, fluorescence by hidden AGN or quasi-stellar object activity, or gravitational cooling.

Key words. galaxies: high-redshift – galaxies: evolution – Galaxy: formation – early Universe

1. Introduction

Lyα emitters (LAEs) are galaxies selected by virtue of their strong Lyα emission. Numerous LAEs have been discovered using the narrowband technique (e.g., Cowie & Hu 1998; Rhoads et al. 2000; Shimasaku et al. 2006; Gronwall et al. 2007; Ouchi et al. 2008, 2010; Cowie et al. 2011; Shibuya et al. 2017) or direct spectroscopic searches (e.g., Shapley et al. 2003; Santos 2004; Rauch et al. 2008; Cassata et al. 2015).

Apart from redshift determinations of high z galaxies (Finkelstein et al. 2013; Schenker et al. 2014; Zitrin et al. 2015), the Lyα line is useful to examine stellar populations of galaxies (e.g., Schaerer 2003; Dijkstra 2014) and can be used to probe the distribution and kinematics of cool gas in and around galaxies (e.g., Mas-Hesse et al. 2003; Verhamme et al. 2006; Steidel et al. 2011). However, interpretations are often complicated because of the intricate radiative transfer of the Lyα line (theoretical studies: e.g., Dijkstra et al. 2006; Laursen et al. 2011; Verhamme et al. 2006, 2012; Gronke et al. 2016; observational studies: e.g., Hayes et al. 2013, 2014; Hashimoto et al. 2015; Herenz et al. 2016).

A widely used tracer of these processes is the rest-frame Lyα equivalent width (EW_0). Based on stellar synthesis models, Schaerer (2003) and Raiter et al. (2010) showed that EW_0 becomes intrinsically larger for galaxies with young stellar ages, low metallicities, or a top-heavy initial mass function (IMF). According to these theoretical studies, it is possible to reproduce values of $EW_0 \lesssim 200$ Å with models of stellar populations with a normal Salpeter IMF (Salpeter 1955) and solar metallicity ($1.0\ Z_\odot$; cf. Charlot & Fall 1993; Malhotra & Rhoads 2002).

According to previous narrowband surveys, a significant fraction of LAEs (10−40%) seem to show very large

$EW_0 \gtrsim 200$ Å (e.g., Malhotra & Rhoads 2002; Shimasaku et al. 2006; Ouchi et al. 2008). Very large EW_0 LAEs are also spectroscopically identified in some studies (e.g., Dawson et al. 2004; Adams et al. 2011; Kashikawa et al. 2012; Hashimoto et al. 2017). According to stellar synthesis models of Schaerer (2003) and Raiter et al. (2010), the very large EW_0 values can be reproduced by either a top-heavy IMF, very young stars ($\lesssim$10 Myr), or very low metallicity stars ($\lesssim$0.02 $Z_\odot$). Thus, very large EW_0 LAEs are important as candidates of galaxies hosting metal-free stars (Population III stars; hereafter PopIII stars). Alternatively, the very large EW_0 values can be reproduced by either Lyα fluorescence due to a hard-ultraviolet spectrum produced by in situ AGN activity or nearby quasi-stellar objects (QSOs; e.g., Malhotra & Rhoads 2002; Cantalupo et al. 2012) or cooling radiation from shock-heated gas (e.g., Rosdahl & Blaizot 2012; Yajima et al. 2012).

However, there are three problems with estimates of EW_0 from previous studies. First, it is now known that Lyα emission is significantly extended compared with UV emission (e.g., Steidel et al. 2011; Hayes et al. 2013; Momose et al. 2014; Wisotzki et al. 2016; Patrício et al. 2016; Sobral et al. 2017; Leclercq et al. 2017). Thus, previous studies had difficulty in estimating total Lyα fluxes. For spectroscopic studies, as Rauch et al. (2008) pointed out, the slit losses can be up to 20–50% of the total fluxes. Second, because LAEs have faint continua, the continuum fluxes are difficult to measure from spectroscopic data. Thus, most studies have estimated continuum fluxes at 1216 Å from broadband photometry in the wavelength range redward of the Lyα line. In this calculation, a flat UV continuum slope, $\beta = -2.0$, is typically assumed, where β is defined as $f_\lambda = \lambda^\beta$ (e.g., Malhotra & Rhoads 2002; Shimasaku et al. 2006; Guaita et al. 2011), although several studies have simultaneously derived β and EW_0 (e.g., Blanc et al. 2011; Jiang et al. 2013; Hashimoto et al. 2017). Therefore, most previous studies suffer from systematic uncertainties in the continuum fluxes at 1216 Å and in EW_0. Finally, a proper association of Lyα emission to UV counterparts is sometimes difficult because of the source crowding in the projected sky. This is particularly the case for ground-based telescopes where the point spread function (PSF) is too large to deblend crowded sources (see also Brinchmann et al. 2017). Wrong associations can cause inaccurate measurements of EW_0. These problems mean that both the narrowband technique and slit spectroscopy suffer from their own shortcomings.

To address these problems, we present a new sample of LAEs obtained from deep observations with the Multi Unit Spectroscopic Explorer (MUSE; Bacon et al. 2010) on the Very Large Telescope (VLT) in the *Hubble* Ultra Deep Field (UDF; Beckwith et al. 2006). The UDF is equipped with extremely deep photometric data, which are useful to constrain accurate continuum fluxes at 1216 Å. The capabilities of this unique integral field unit (IFU) spectrograph, in particular its high sensitivity and spectral/spatial resolution, together with the HST data enable us to produce a homogeneous sample of faint LAEs with unprecedented depth.

In this study, we focus on two controversial issues: first, the evolution of the EW_0 distribution between $z = 2.9$ and 6.6, and second, the existence of very large EW_0 LAEs.

Regarding the first point, many observational studies have examined the EW_0 distribution, and several of these studies have also investigated the evolution of the distribution. The distribution is often expressed as an exponential law $N = N_0 \exp(-EW_0/w_0)$, where w_0 is the scale factor of EW_0 (e.g., Gronwall et al. 2007; Nilsson et al. 2009; Guaita et al. 2010; Ciardullo et al. 2012; Zheng & Wallace 2014; Oyarzún et al. 2016, 2017; Shibuya et al. 2017). Based on a compiled sample of LAEs at $0 < z < 6$ from the literature, Zheng et al. (2014) claimed that w_0 becomes large at high z (see also Ciardullo et al. 2012 who found similar redshift evolution at $2 < z < 3$). These results suggest that large EW_0 LAEs are more common at higher z, which may be consistent with the evolution of the fraction of strong Lyα emission among dropout galaxies (e.g., Stark et al. 2010; Cassata et al. 2015). However, the results on the redshift evolution are based on a compiled sample that comprises LAEs with various selection functions (i.e., limiting EW_0 and UV magnitudes). Thus, it is crucial to investigate whether the selection functions of LAEs affect the EW_0 distribution results. This is important because previous observational studies have pointed out that fainter continuum objects have larger EW_0 values, the so-called Ando effect (e.g., Ando et al. 2006; Stark et al. 2010; Furusawa et al. 2016). With our MUSE LAE sample, we examine the EW_0 distribution and its redshift evolution between $z = 2.9$ and 6.6.

This paper is organized as follows. We describe our data and LAE sample in Sect. 2. In Sect. 3, we derive UV continuum slopes (β) and UV absolute magnitudes ($M_{\rm UV}$) of our LAEs. In this section, a correlation between $M_{\rm UV}$ and β and the redshift evolution of β are presented. In Sect. 4, we derive Lyα fluxes based on the curve of growth technique and examine AGN activity of our LAE sample in Sect. 5. In Sect. 6. we show the EW_0 distribution and its redshift evolution. The Ando effect is examined in Sect. 7, followed by properties of very large EW_0 LAEs in Sect. 8. Discussion in the context of EW_0 and comparisons between observations and theoretical studies are presented in Sect. 9, and our summary and conclusions are presented in Sect. 10. Throughout this paper, magnitudes are given in the AB system (Oke & Gunn 1983) and we assume a Λ cold dark matter cosmology with $\Omega_{\rm m} = 0.3$, $\Omega_\Lambda = 0.7$ and $H_0 = 70\ {\rm km\,s^{-1}\ Mpc^{-1}}$.

2. Data and sample

2.1. Spectroscopy with MUSE

We carried out observations with MUSE in the UDF between September 2014 and February 2016 under the MUSE consortium GTO (PI: R. Bacon). The wavelength range of MUSE is 4750–9300 Å and the typical instrumental spectral resolution is $R \sim 3000$. Bacon et al. (2017; hereafter B17) provide more details about the observations and data reduction. Briefly, the UDF was observed with MUSE in two different integration times (see Fig. 1 in B17). The mosaic field is the medium deep region consisting of nine pointings of 1 arcmin^2 (9 arcmin^2 in total). In this region, each pointing has a 10 h exposure time. The udf-10 field is the ultra deep region, covering 1 arcmin^2. In this region, the total exposure time is 31 h. The spatial scale is $0\farcs2 \times 0\farcs2$ per spatial pixel and the spectral sampling is 1.25 Å per spectral pixel.

2.2. Source extractions

The source extraction of objects and the construction of the parent catalog are given in B17 and Inami et al. (2017; hereafter I17). In short, objects were detected and extracted using two methods.

The first method uses the catalog of Rafelski et al. (2015) as a positional prior. In Rafelski et al. (2015), photometry has been performed for 9927 objects in the UDF with the latest and

the deepest HST data covering the wavelength ranges from far ultraviolet (FUV) to near-infrared (NIR). Using the sky coordinates of each object from the catalog of Rafelski et al. (2015), we searched for spectral features (absorption or emission lines).

The second method is based on our custom made software ORIGIN (Mary et al., in prep.). ORIGIN blindly searches for emission line objects (see B17 for the detail). The strength of ORIGIN is that we can detect emission line objects without HST images as positional priors. The ORIGIN-only objects without HST counterparts are candidates for very large EW_0 LAEs. This is because non-detections of HST images indicate that their continuum fluxes are extremely faint, increasing their EW_0. These objects are presented in B17 and their properties will be presented elsewhere.

2.3. Parent Lyα emitters sample

The parent LAE sample was constructed by I17 with the following two criteria:

- We selected LAEs with secure redshifts $2.9 < z < 6.6$ ("TYPE = 6" and "CONFID = 2 and 3").
- As we describe in detail in Sect. 4, we created continuum-subtracted narrowband images of Lyα emission in the same way as in Drake et al. (2017b,a; hereafter D17). Based on the narrowband images, we estimated Lyα fluxes and errors (see Sect. 4.1). We imposed a minimum signal-to-noise ratio (S/N) in Lyα flux of 5. The minimum S/N adopted in the present study is slightly lower than the $S/N = 6$ used in Leclercq et al. (2017; hereafter L17). The higher S/N limit is important in L17 because their goal is to detect diffuse faint Lyα emission on an individual basis. In this study, we chose the S/N cut of 5 to increase the number of LAEs.

A fraction of LAEs in the udf-10 field are also detected in the mosaic field. In these overlapped cases, we adopted the results in the udf-10 field because this field is deeper than the mosaic in Lyα. After removing those overlapped objects, there are 156 and 526 parent LAEs in the udf-10 and mosaic fields, respectively.

For these objects, we performed visual inspection. In this procedure, we first removed spurious objects[1] and next removed LAEs with close companion LAEs whose individual Lyα fluxes are affected by the companions' Lyα fluxes. In total, 11 objects were removed from the sample.

2.4. Our Lyα emitters selected with MUSE and public HST data

For robust estimates of EW_0, it is important to obtain accurate continuum fluxes at 1216 Å. As can be seen in Fig. 9 of Bacon et al. (2015) and in Fig. 12 of B17, despite the high sensitivity of MUSE, it is difficult to precisely determine continuum fluxes for faint objects.

Therefore, we used the public HST photometry catalog of Rafelski et al. (2015). We describe the HST data in Sect. 2.4.1 and then construct our final LAE sample in Sect. 2.4.2.

2.4.1. Public HST data

The catalog of Rafelski et al. (2015) is the same as the catalog we used as a positional prior for source extractions (Sect. 2.2). At $z \sim 2.9$–6.6, the rest-frame FUV continuum roughly corresponds to 8000–16 000 Å in the observed frame. Thus, we used the public HST data from F775W to F160W depending on the redshifts of the objects. Table A.1 summarizes the public HST photometry data used in this study.

For the objects detected with the positional priors, we used total magnitudes from Rafelski et al. (2015). The total magnitudes were obtained from the Kron radius (Kron 1980) and were carefully corrected for aperture-matched PSFs and Galactic extinction. For the objects detected only by ORIGIN, we performed our own photometric analysis using NoiseChisel developed by Akhlaghi & Ichikawa (2015; see B17 for the procedure).

2.4.2. Our Lyα emitters sample

One has to take the PSF difference into account to fairly compare HST data with MUSE data. As described in B17 and I17, the segmentation maps of MUSE data cubes were based on the segmentation map of HST data (Rafelski et al. 2015) convolved with the MUSE PSF, typically $FWHM \approx 0\farcs6$ (see the top panel of Fig. 7 in B17). The B17 and I17 works carefully assigned each MUSE-detected object to an HST counterpart. To do so, B17 and I17 examined the narrowband images. In this procedure, 78 LAEs were found to have more than one HST counterparts. These objects were removed from our sample to obtain a clean sample. For the rest of the sample with a single HST counterpart, we could directly compare MUSE-based Lyα fluxes with HST-based continuum fluxes.

As we describe in detail in Sect. 3, we used two or three HST wave bands to derive UV continuum slopes. Therefore, we also applied the following HST detection criterion to our LAEs: at least two HST bands are detected above 2σ. The typical 2σ limiting magnitudes within $0\farcs2$ radius apertures correspond to apparent magnitudes of 29.2–31.1 (see Table A.1).

After imposing this criterion on our objects, we are left with 80 and 337 LAEs in the udf-10 and mosaic fields, respectively. The redshift distribution of the two fields are shown in the left panel of Fig. 1. For the remainder of the present paper, we use the sample with HST detections above 2σ. Table 1 summarizes our LAE sample.

We discuss possible bias effects due to our selection technique in Sect. 9.1.

3. Ultraviolet continuum properties obtained with HST

3.1. Ultraviolet magnitudes and continuum slopes

Ultraviolet continuum slopes are estimated by fitting two or three HST magnitudes. From the definition of UV continuum slopes, $f_\lambda \propto \lambda^\beta$, the relation between AB magnitudes and wavelengths in Å is expressed as

$$\mathrm{mag} = -2.5\log(\lambda^{\beta+2}) + A, \quad (1)$$

where A is a constant corresponding to the amplitude. We chose passbands so that Lyα emission or intergalactic medium (IGM) absorption do not affect the photometry. In order to calculate β values as uniform as possible at rest-frame wavelengths, we divided our LAEs into three redshift bins based on their spectroscopic redshifts, $z_{\rm sp}$: $2.90 \leqq z_{\rm sp} \leqq 4.44$, $4.44 < z_{\rm sp} \leqq 5.58$, and $5.58 < z_{\rm sp} \leqq 6.66$, with mean redshifts of $z = 3.6$, 4.9, and 6.0, respectively. The number of LAEs in each redshift bin are listed in Table 1, and the relevant HST filters are listed in

[1] These include LAEs with OH sky line contamination and with the noisy Lyα lines.

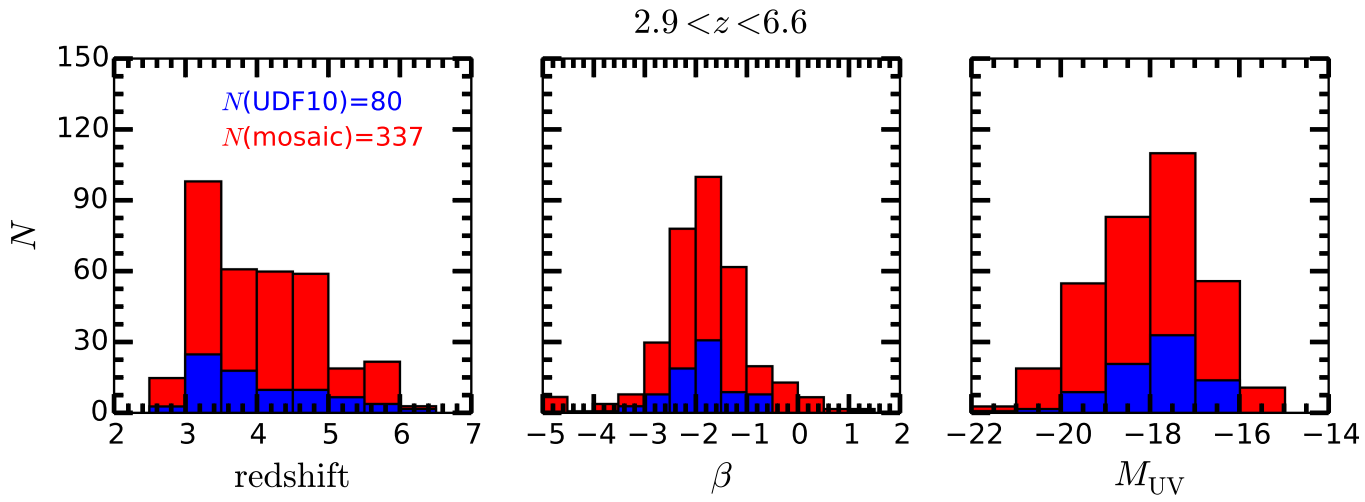


Fig. 1. *Left, middle, and right panels*: distributions of z, β and $M_{\rm UV}$ for the entire sample at $2.9 < z < 6.6$, respectively. In each panel, the blue and red histograms correspond to the distributions for udf-10 and mosaic, respectively. A two-sample Kolmogorov-Smirnov test (K-S test) results in the p-value of 0.84, 0.25, and 0.32 for the two z, β and $M_{\rm UV}$ distributions, respectively, indicating that the distributions of the values in the two fields cannot be distinguished from each other.

Table 1. Summary of our LAE sample.

Field	$N_{\rm tot}$	$N_{\rm analyzed}$	$\langle z\rangle = 3.6$	$\langle z\rangle = 4.9$	$\langle z\rangle = 6.0$
udf-10	156	80	56	18	6
mosaic	526	337	224	90	23
Total	682	417	280	108	29

Notes. $N_{\rm tot}$ denotes the total number of spectroscopic LAEs in I17 that have secure redshifts and Lyα flux $S/N > 5.0$. $N_{\rm analyzed}$ is the number of LAEs analyzed in this paper. Numbers denote samples with HST detections above 2σ in HST wave bands listed in Table 2.

Table 2. With the typical wavelengths of the filters, our β values probe UV continuum slopes in the rest-frame wavelength ranges of ∼1700−2400 Å, which are consistent with those in Bouwens et al. (2009): 1600−2300 Å. Typically we used three filter bands to determine β. However, owing to the limited spatial coverage of F140W, the determination of β rely on the remaining two filters for some objects. We checked and confirmed that the β measurements are not statistically affected by the lack of F140W[2].

With β and A values in Eq. (1), we estimate apparent magnitudes at 1500 Å, m_{1500}, as follows:

$$m_{1500} = -2.5\log(\{1500\times(1+z_{\rm sp})\}^{\beta+2}) + A. \quad (2)$$

From m_{1500}, we obtain $M_{\rm UV}$ as

$$M_{\rm UV} = m_{1500} - 5\log(d_L/10\ {\rm pc}) + 2.5\log(1+z_{\rm sp}), \quad (3)$$

where d_L indicates the luminosity distance in parsec (pc) corresponding to the spectroscopic redshift, $z_{\rm sp}$, derived in I17.

We estimate apparent magnitudes at 1216 Å, m_{1216}, as in Eq. (2). Using m_{1216}, we obtain continuum fluxes at 1216 Å in erg cm^{-2} s^{-1} Hz^{-1}, $f_{\nu,{\rm cont}}$, from the relation

$$f_{\nu,{\rm cont}} = 10^{-0.4(m_{1216}+48.6)}. \quad (4)$$

Finally, we derive $f_{\lambda,{\rm cont}}$ from $f_{\nu,{\rm cont}}$ as follows:

$$f_{\lambda,{\rm cont}} = f_{\nu,{\rm cont}} \times \frac{c}{\{1216(1+z_{\rm sp})\}^2}, \quad (5)$$

where c is the speed of light in Å s^{-1}.

To estimate the physical quantities and their errors, we applied a Monte Carlo technique as we describe below. With HST magnitudes and their errors, we generated 300 mock magnitudes for each passband listed in Table 2 under the assumption that the magnitude distribution is a Gaussian. We take the low-z bin as an example. With 300 sets of mock magnitudes, F775W, F850LP, and F105W, we derive 300 sets of β and A values with Eq. (1). We then obtain 300 sets of $M_{\rm UV}$ and $f_{\lambda,{\rm cont}}$ from Eqs. (2)−(5). The median and standard deviation of the distribution of measurements are adopted as the measured and error values, respectively.

The middle panel of Fig. 1 shows the β distribution for the entire sample of LAEs. The β values range from −5 to 1 with a median value of −1.81. The values $\beta \lesssim -3$ are physically unlikely (e.g., Schaerer 2003). We find that objects with very steep values, for example, $\beta \lesssim -3$, have uncertainties on β as large as 1.0. For the combined sample of LAEs in the udf-10 and mosaic fields, we calculated the mean, median, standard deviation, and standard error values for each redshift bin. These values are listed in Table 3.

[2] The lack of F140W can affect the results at $z \sim 4.9$ and 6.0 (see Table 2). Basically, most udf-10 LAEs are in the coverage of F140W. Thus, using these LAEs, we derive two β values: with and without F140W. To evaluate the effect, we performed the Kormogorov-Smirnov (K-S) test for the two β distributions. We obtain the p values of 0.36 and 0.99 for $z \sim 4.9$ and 6.6, respectively, indicating that the β distributions cannot be distinguished from each other. However, the uncertainties in β measurements become smaller if we include F140W.

Table 2. Wave bands used to derive the UV continuum slope for individual galaxies.

Redshift range (1)	Mean redshift (2)	Filters (3)	Rest-frame wavelengths (Å) (4)
$2.90 \leqq z_{\rm sp} \leqq 4.44$	3.6	*F775W*, *F850LP*, *F105W*	1700–2300
$4.44 < z_{\rm sp} \leqq 5.58$	4.9	*F105W*, *F125W*, *F140W*[a]	1800–2100 (1800–2400)[b]
$5.58 < z_{\rm sp} \leqq 6.66$	6.0	*F125W*, *F140W*[a] , *F160W*	1800–2200

Notes. (1) Spectroscopic redshift ranges of the three redshift bins. (2) Mean redshift of each redshift bin. (3) HST filters used to estimate UV continuum slopes. (4) Typical rest-frame wavelengths probed by UV continuum slopes. [(a)] F140W is used if it is available. [(b)] Value in the parenthesis is the wavelength range in the case that F140W is available.

Table 3. Summary of physical quantities.

Quantity (1)	z (2)	N (3)	Mean (4)	Median (5)	σ (6)	$\sigma/\sqrt{N}$ (7)
β	3.6	280	−1.62	−1.73	0.72	0.04
	4.9	108	−2.17	−2.22	1.57	0.15
	6.0	29	−2.10	−2.321	1.05	0.19
$M_{\rm UV}$	3.6	280	−17.7	−17.6	1.1	0.1
	4.9	108	−18.4	−18.4	1.0	0.1
	6.0	29	−19.1	−19.0	1.1	0.2
$L_{{\rm Ly}\alpha}$	3.6	280	41.9	41.9	0.4	0.1
	4.9	108	42.1	42.0	0.4	0.1
	6.0	29	42.5	42.5	0.4	0.1
EW_0	3.6	280	113	87	96	6
	4.9	108	83	57	88	8
	6.0	29	130	97	120	22

Notes. (1) Physical quantity; (2) redshift of the sample; (3) number of objects; (4)–(7) mean, median, standard deviation, and standard error values.

The right panel of Fig. 1 shows the $M_{\rm UV}$ distribution for our LAEs. The median value, −17.9, is more than two orders of magnitude fainter than previous high z LAE studies based on the narrowband technique (Shimasaku et al. 2006; Ouchi et al. 2008) and spectroscopy (Stark et al. 2010; Cassata et al. 2015). The typical $M_{\rm UV}$ value in these studies is roughly −20.5. In our LAE sample selection, we included all objects with HST detections above 2σ in multiple wave bands. The corresponding lowest $M_{\rm UV}$ values are ∼−16, −17, and −18 at $z \sim 3.6$, 4.9, and 6.6, respectively.

3.2. Correlation between $M_{\rm UV}$ and β

For dropout galaxies, a uniform picture has emerged that β values become steeper at fainter $M_{\rm UV}$ at various redshifts from $z \sim 1$ to 8 (e.g., Bouwens et al. 2009, 2012, 2014; Wilkins et al. 2011; Kurczynski et al. 2014). While Finkelstein et al. (2012), Dunlop et al. (2012), Hathi et al. (2016) claimed that the correlation is not clear, Kurczynski et al. (2014), Bouwens et al. (2014), Rogers et al. (2014) showed that the discrepant results are due to systematics and biases. Once corrected for these systematics and biases, the slope is consistently $d\beta/dM_{\rm UV} \approx -0.10$. Since β values become steeper if the dust content is low (Meurer et al. 1999), this anti-correlation is interpreted as fainter $M_{\rm UV}$ galaxies having lower dust contents.

Several previous studies examined β in LAEs at $3 < z < 7$ (e.g., Ouchi et al. 2008; Ono et al. 2010; Stark et al. 2010; Jiang et al. 2013). However, compared to the typical magnitude range of the dropout galaxies, $-22 < M_{\rm UV} < -15$, the magnitude range in the LAE studies is narrow, $-22 < M_{\rm UV} < -19$. Because our LAEs have a UV magnitude range that is comparable to that for dropout galaxies, $-22 < M_{\rm UV} < -16$, we compared our β values with those of dropout galaxies.

Figure 2 plots β against $M_{\rm UV}$ for our individual LAEs. To quantify the relation, we calculated the biweight mean of β at each magnitude bin (cf. Bouwens et al. 2012, 2014). The biweight mean and error values are listed in Table 4. We fit the biweight mean values with a linear function. The slopes are $d\beta/dM_{\rm UV} = -0.09 \pm 0.03$, -0.10 ± 0.06, and -0.04 ± 0.15 for $z \sim 3.6$, 4.9, and 6.0, respectively. From Fig. 2, we see that β values become steeper at fainter $M_{\rm UV}$, in agreement with the previous findings of Bouwens et al. (2012).

In Fig. 3, we compare our $d\beta/dM_{\rm UV}$ values with those of dropout galaxies (Bouwens et al. 2009, 2014; Finkelstein et al. 2012; Kurczynski et al. 2014). We find that our $d\beta/dM_{\rm UV}$ of LAEs are in good agreement with previous studies of dropout galaxies. These results therefore indicate that fainter UV continuum LAEs have lower dust contents.

3.3. Redshift evolution of β

Previous studies on continuum-selected galaxies have shown that β values become steep at high z (Bouwens et al. 2009, 2014; Dunlop et al. 2012; Finkelstein et al. 2012; Hathi et al. 2013; Kurczynski et al. 2014). Since we derived β values in a uniform manner at $2.9 < z < 6.6$, it is interesting to see if LAEs have a similar redshift evolution in β. Figure 4 shows the redshift evolution of β for our LAEs. We also include data points of dropout galaxies in the literature mentioned above. To perform fair comparisons of β at various redshifts, we investigated β evolutions in two $M_{\rm UV}$ bins, ∼−19.5 and −17.5. These $M_{\rm UV}$ values correspond to 0.25 and 0.05 $L^*_{z=3}$, respectively, where $L^*_{z=3}$ is −21.07

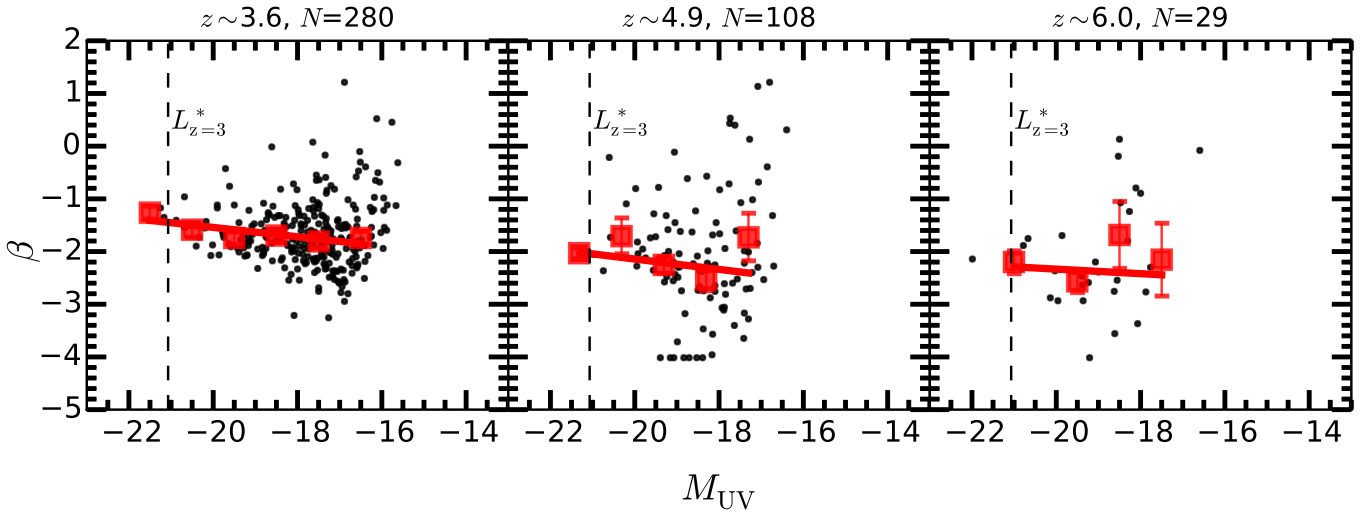


Fig. 2. *From left to right*: β plotted against $M_{\rm UV}$ for $z \sim 3.6$, 4.9, and 6.0. The small black circles indicate individual LAEs. The vertical dashed line indicates the characteristic UV luminosity at $z \sim 3$, $L^*_{z=3} = -21.07$ (Steidel et al. 1999). The red squares show biweight mean values of β at each $M_{\rm UV}$ bin. The biweight mean is a robust statistic for determining the central location of a distribution. The standard deviation of the biweight mean is determined based on bootstrap simulations at each magnitude bin. The solid red line is the best-fit linear function to the biweight mean values. The slopes are $d\beta/dM_{\rm UV} = -0.09 \pm 0.03$, -0.10 ± 0.06, and -0.04 ± 0.15 for $z \sim 3.6$, 4.9, and 6.0, respectively.

Table 4. Biweight mean of physical quantities as a function of ultraviolet luminosity.

$M_{\rm UV}$ (1)	log $L_{{\rm Ly}\alpha}$ (2)	β (3)	EW_0 (4)	N (5)
		$z \sim 3.6$		
−21.5	42.0 ± 0.7	−1.26 ± 0.07	32 ± 14	2
−20.5	42.4 ± 0.3	−1.58 ± 0.10	23 ± 10	11
−19.5	42.3 ± 0.1	−1.74 ± 0.07	44 ± 6	29
−18.5	42.1 ± 0.1	−1.69 ± 0.07	65 ± 7	57
−17.5	41.9 ± 0.1	−1.80 ± 0.06	90 ± 6	107
−16.5	41.7 ± 0.1	−1.74 ± 0.07	140 ± 12	63
		$z \sim 4.9$		
−21.5	43.3 ± 0.1	−2.02 ± 0.01	85 ± 19	2
−20.5	42.4 ± 0.1	−1.70 ± 0.33	32 ± 9	9
−19.5	42.3 ± 0.1	−2.24 ± 0.12	47 ± 8	31
−18.5	42.0 ± 0.1	−2.53 ± 0.19	46 ± 8	35
−17.5	41.8 ± 0.1	−1.72 ± 0.44	78 ± 16	27
		$z \sim 6.0$		
−21.0	42.6 ± 0.2	−2.19 ± 0.20	24 ± 8	6
−19.5	42.6 ± 0.2	−2.55 ± 0.19	91 ± 39	9
−18.5	42.5 ± 0.1	−1.68 ± 0.63	173 ± 49	10
−17.5	42.4 ± 0.2	−2.15 ± 0.68	155 ± 134	3

Notes. The uncertainty values are the standard errors derived based on bootstrap simulations. The values represent how the median values are well constrained.

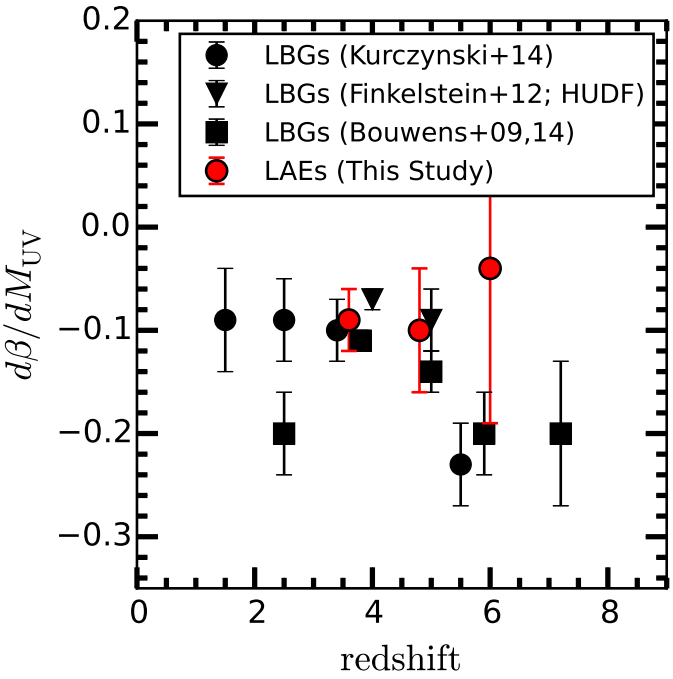


Fig. 3. Derivative of β with UV magnitude plotted against redshift, z. Our LAEs, denoted as red circles, are placed at mean redshifts $z \sim 3.6$, 4.9, and 6.6.

(Steidel et al. 1999). We chose these $M_{\rm UV}$ values to compare our results with those in Kurczynski et al. (2014) who used the same $M_{\rm UV}$ bins.

There are two results in Fig. 4. First, we find that our β values are consistent with those in dropouts within 1σ uncertainties at a given $M_{\rm UV}$. At first glance, the result is at odds with the result of Stark et al. (2010). These authors found that dropout galaxies with Lyα emission have steeper β compared with those without Lyα emission at the UV magnitude range from −21.5 to −20.0. However, as can be seen from Fig. 14 in Stark et al. (2010), the β difference becomes negligible in their faintest bin, $M_{\rm UV} = -20.0$. Therefore, given the very faint $M_{\rm UV}$ of our LAEs (see Fig. 1), it is not surprising that our LAEs and dropout galaxies have similar β. Second, we see a trend that β becomes steeper at higher z in LAEs, at least at bright $M_{\rm UV}$. This trend is also consistent with that in dropouts, indicating that the dust contents of LAEs is low at high z.

To summarize this section, we presented UV continuum properties of our LAEs, which cover a wide range of $M_{\rm UV}$. We demonstrated that β values in LAEs are in good agreement with those in dropout galaxies at a given redshift or $M_{\rm UV}$. The results indicate that dust contents become smaller for higher z and fainter $M_{\rm UV}$ galaxies.

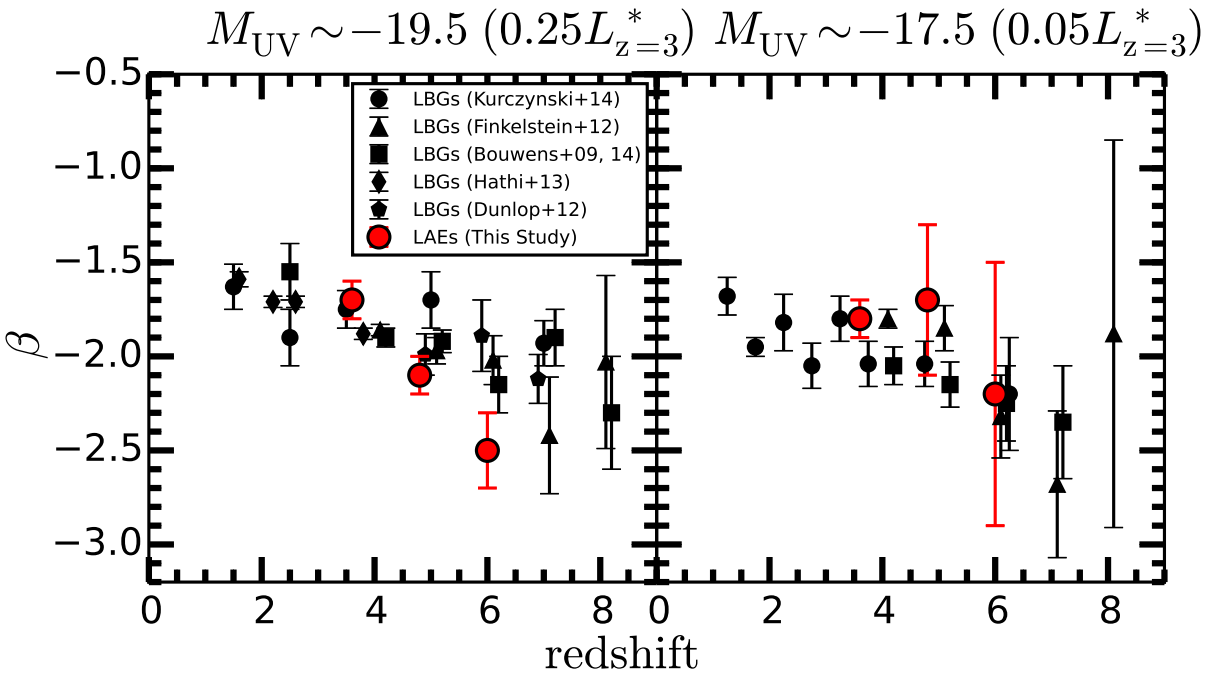


Fig. 4. *Left and right panels*: redshift evolution of β values at bright ($M_{\rm UV}\sim-19.5$) and faint ($M_{\rm UV}\sim-17.5$) UV absolute magnitudes, respectively.

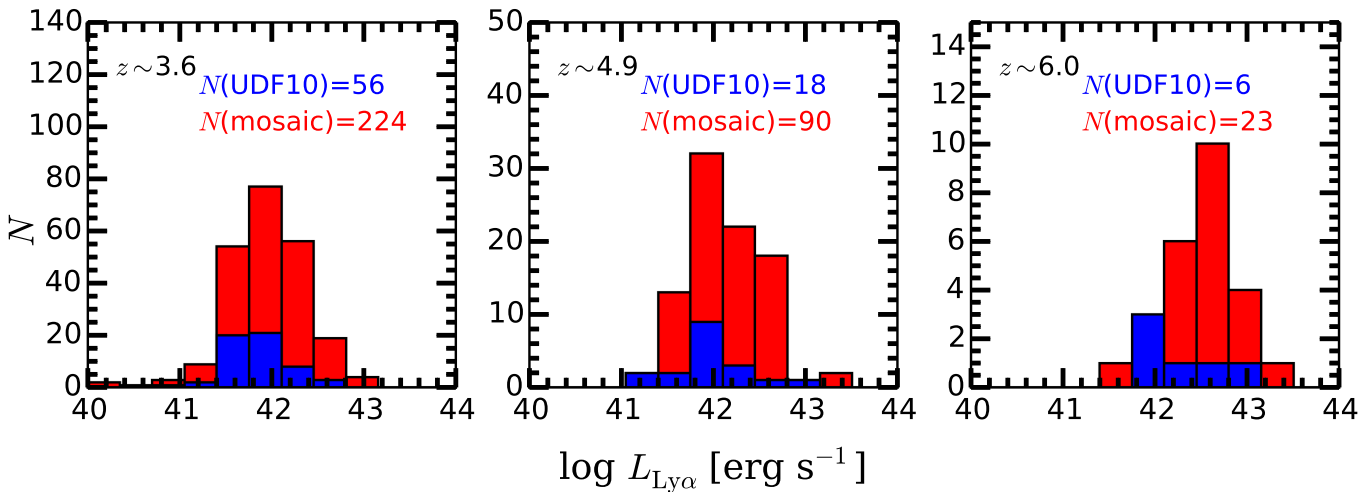


Fig. 5. *From left to right*: Lyα luminosity distributions for $z\sim3.6$, 4.9, and 6.0. The blue and red histograms correspond to the distributions for udf-10 and mosaic, respectively. Two sample K-S tests result in p values of 0.01, 0.34, and 0.08 for $z\sim3.6$, 4.9, and 6.0, respectively, indicating that the distributions of $L_{\rm Ly\alpha}$ values in the two fields are statistically different from one another at least at $z\sim3.6$.

4. Accurate Lyα fluxes obtained with MUSE

4.1. Measurements of Lyα fluxes

Wisotzki et al. (2016) and L17 have shown that Lyα emission is significantly extended compared with UV emission not only statistically but also for individual objects. To capture the extended Lyα flux, we adopted the curve of growth technique in the same manner as in Wisotzki et al. (2016), Drake et al. (2017b,a), Leclercq et al. (2017). The detailed procedure is provided in Sect. 3 of D17. Briefly, we performed photometry on the Lyα narrowband images after subtracting the local background and masking out nearby objects. We applied various sizes of annuli until the curve of growth reaches the background level. The cumulative flux is adopted as the total Lyα flux, while the error flux is estimated from the variance cube.

We note that our Lyα fluxes are not corrected for the Galactic extinction. However, correction factors would be very small in the UDF as we describe below. In the UDF, Rafelski et al. (2015) have investigated the Galactic extinction. In the *F606W* and *F775W* bands, whose wavelengths coverage matches those of our Lyα lines, the Galactic extinction values are 0.023 and 0.016, respectively. These differences in magnitudes correspond to ~2% differences in fluxes. Therefore, regardless of the correction for the Galactic extinction, our results remain unchanged.

Figure 5 shows the distribution of Lyα luminosities, $L_{\rm Ly\alpha}$, for our LAEs. The $L_{\rm Ly\alpha}$ values span the range from $\log(L_{\rm Ly\alpha}/{\rm erg\ s^{-1}})\approx41.0$ to 43.0. Because we obtained deeper data in udf-10 than in mosaic, we investigated the Lyα depth difference in the two fields. We found that the mean Lyα flux in udf-10 is 1.3, 1.3, and 2.0 times fainter than in mosaic at $z\sim3.6$,

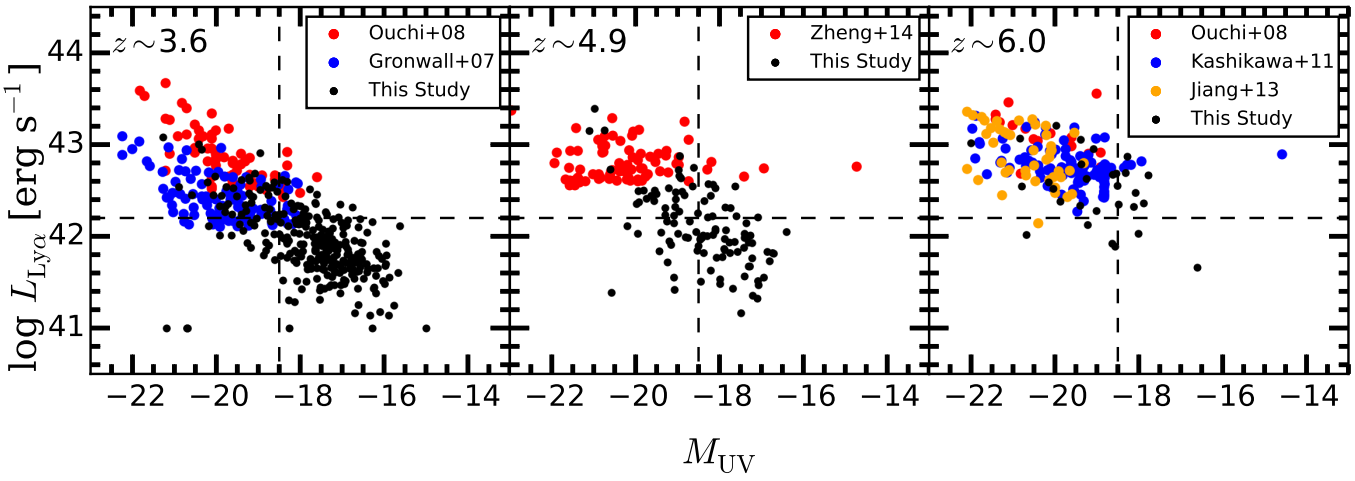


Fig. 6. *From left to right*: log $L_{Ly\alpha}$ plotted against M_{UV} for $z \sim 3.6$, 4.9, and 6.0. The black circles indicate our individual LAEs. In each panel, objects with log ($L_{Ly\alpha}$/erg s^{-1}) < 41.0 are placed at 41.0 for display purposes. *Left panel*: red circles show spectroscopically confirmed LAEs from Ouchi et al. (2008) at $z \sim 3.1$ and 3.7, while blue circles indicate a photometric LAE sample from Gronwall et al. (2007). *Middle panel*: red circles correspond to $z \sim 4.5$ LAEs studied by Zheng et al. (2014). *Right panel*: red circles show spectroscopically confirmed LAEs from Ouchi et al. (2008) at $z \sim 5.7$. Blue circles indicate spectroscopically confirmed LAEs from Kashikawa et al. (2011) at $z \sim 5.7$ and 6.5, while orange circles are spectroscopically confirmed LAEs from Jiang et al. (2013) at $z \sim 5.7$, 6.5, and 7.0. In each panel, the vertical dashed line at $M_{UV} = -18.5$ and the horizontal dashed line at log ($L_{Ly\alpha}$/erg s^{-1}) = 42.2 show the cuts used for fair comparisons of EW_0 scale lengths at $2.9 < z < 6.6$ (see Sect. 6.3).

4.9, and 6.0, respectively[3]. The mean, median, standard deviation, and standard error values for the entire sample are listed in Table 3.

4.2. M_{UV} and $L_{Ly\alpha}$

In order to demonstrate the power of MUSE and the uniqueness of our sample, we compare our M_{UV} and $L_{Ly\alpha}$ with those in the literature in Fig. 6. As can be seen from the figure, our LAEs are fainter in both M_{UV} and $L_{Ly\alpha}$ than those in previous studies. In particular, at $z \sim 3.6$ and 4.9, lower ends of continuum and Lyα fluxes are about an order of magnitude fainter than previous studies. At $z \sim 6.0$, the magnitude (luminosity) difference is small between this study and the literature. This would be due to the small statistics at $z \sim 6.0$ and because strong sky fluxes prevent us from detecting faint objects at $z \sim 6.0$ (see Fig. 5 in D17).

Figure 6 also shows that brighter M_{UV} objects have larger $L_{Ly\alpha}$. This trend is expected because both M_{UV} and $L_{Ly\alpha}$ values increase with the star formation rates (see also Matthee et al. 2017).

5. AGN activity in the sample

It is known that AGN activity can also generate Lyα emission as a result of ionizing photon radiation from AGNs (e.g., Malhotra & Rhoads 2002). Based on X-ray emission and high-ionization state emission lines (e.g., CIV λ1549 and HeII λ1640), previous studies have shown that the AGN fraction among LAEs is as low as 0–2% at $z > 3$ (e.g., Malhotra et al. 2003; Gawiser et al. 2006; Ouchi et al. 2008). If this is the case, we expect 0–10 AGNs among the present sample. Since we are interested in LAEs whose Lyα emission is powered by star formation activity, we need to remove AGN-like LAEs from the sample.

To do so, we first compared the sky coordinates of our LAEs with those in a very deep (7 Ms) archival X-ray catalog (Luo et al. 2017). The X-ray catalog includes objects detected in up to three X-ray bands: 0.5–7.0 keV, 0.5–2.0 keV, and 2–7 keV. The average flux limits close to the HUDF are 1.9×10^{-17}, 6.4×10^{-18}, and 2.7×10^{-17} erg cm^{-2} s^{-1} in the three X-ray bands. Following the procedure in Herenz et al. (2017), a cross-matching is regarded as successful if an LAE has a counterpart within an aperture. We adopted the aperture size of three times the X-ray positional error, which is the same aperture size as adopted in Herenz et al. (2017). We found that an AGN-LAE: LAE (AGN) ID is 6565 (758), where AGN ID is taken from Luo et al. (2017). The AGN has not been spectroscopically identified in previous searches for optical counterparts of AGNs. We listed the object in Table 5 and removed it from the sample.

Secondly, we made use of Lyα luminosities, $L_{Ly\alpha}$. Recently, Konno et al. (2016) have examined $L_{Ly\alpha}$ of LAEs at $z \sim 2$. The authors have revealed that bright LAEs with log ($L_{Ly\alpha}$/erg s^{-1}) > 43.4 have X-ray or radio counterparts. Thus, Konno et al. (2016) have concluded that very bright LAEs at $z \sim 2$ are AGNs. Based on this result, we regard an LAE to be an AGN if log L(Lyα/erg s^{-1}) > 43.4. None of our LAEs satisfy this criterion.

Finally, we assessed the full width half maxima (FWHM) of Lyα spectral lines in the catalog presented in I17. It is expected that Type 1 AGNs have broad Lyα emission lines. None of our LAEs have FWHM values larger than 1000 km s^{-1}.

We conclude that there is at least one obvious Type 1 AGN in our LAE sample. In addition, hidden Type 2 AGNs may present among the sample.

6. Distribution of Lyα equivalent widths and its evolution

6.1. Measurements of Lyα equivalent widths and scale lengths

To derive EW_0 and standard deviation values for each object, we performed Monte Carlo simulations. To do so, we first generated 300 sets of continuum fluxes at 1216 Å and $F_{Ly\alpha}$ based on the assumption that the distributions are Gaussian with mean and

[3] These correspond to the log ($L_{Ly\alpha}$/erg s^{-1}) difference of 0.1, 0.1, and 0.3 at $z \sim 3.6$, 4.9, and 6.0, respectively.

Table 5. Properties of a X-ray detected AGN-like LAE.

MUSE ID (1)	Chandra 7 Ms ID (2)	z (3)	EW_0 (4)	log $L_{Ly\alpha}$ (5)	M_{UV} (6)	β (7)	$FWHM(Ly\alpha)$ (8)
6565	758	3.20	132 ± 116	41.6 ± 0.4	-16.4 ± 0.2	-1.9 ± 0.4	209 ± 15

Notes. ID and physical quantities of an AGN-LAE whose optical counterpart has not been identified in previous studies. Chandra 7 Ms IDs are taken from Luo et al. (2017).

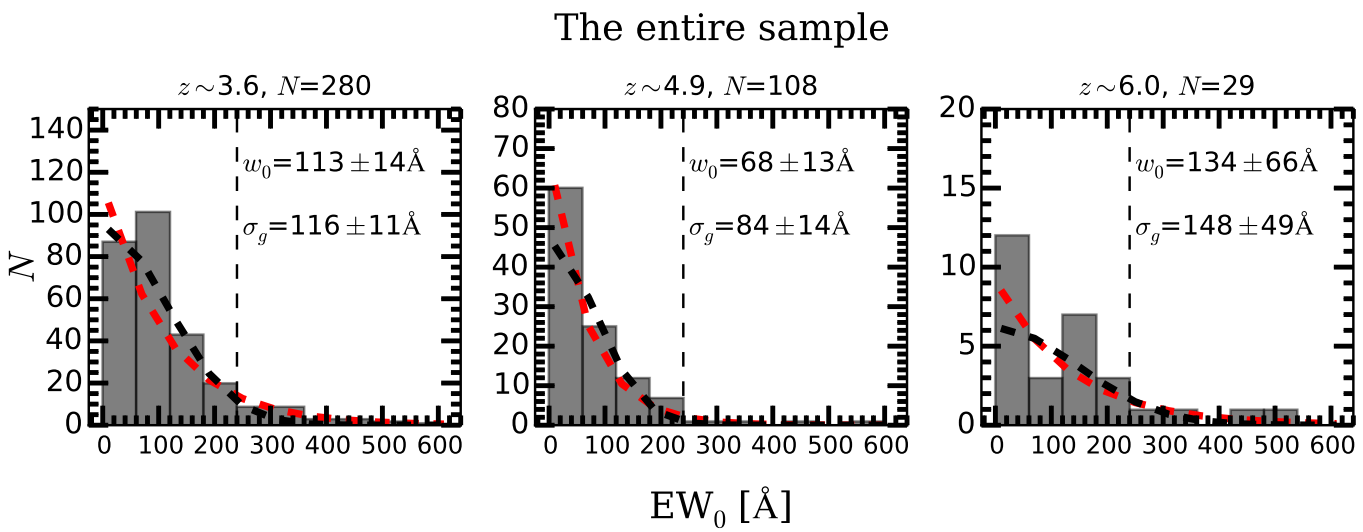


Fig. 7. *From left to right*: EW_0 distributions for $z \sim 3.6$, 4.9, and 6.0 with a bin width of 60 Å (gray histograms). One (one) object at $z \sim 3.6$ (4.9) with $EW_0 > 600$ Å is placed at $EW_0 = 600$ Å for display purposes. The vertical dashed line indicates $EW_0 = 240$ Å (cf. Schaerer 2003; Raiter et al. 2010). The red dashed lines show the best-fit curves of the distributions expressed as $N = N_0 \exp(-EW_0/w_0)$, where w_0 indicates the best-fit scale factor. The black dashed lines indicate the best-fit curves of the distributions expressed as $N = N_0 \exp(-EW_0{}^2/2\sigma_g^2)$, where σ_g indicates the best-fit distribution width.

standard deviation values derived in Sects. 3.1 and 4.1, respectively. We then obtained 300 sets of EW_0 as follows:

$$EW_0 = \frac{F_{Ly\alpha}}{f_{\lambda,\mathrm{cont}}} \times \frac{1}{(1+z_{\mathrm{sp}})}. \quad (6)$$

For each object, the mean and standard deviation of the distribution of measurements are adopted as the measured and error values, respectively. In Table 3, we list the mean, median, standard deviation, and standard error values of EW_0 for our entire sample.

Figure 7 shows the EW_0 distribution for our LAEs. It is known that the EW_0 distribution can be described either with an exponential law, $N = N_0 \exp(-EW_0/w_0)$ (Gronwall et al. 2007; Nilsson et al. 2009; Guaita et al. 2010; Zheng et al. 2014), or with a Gaussian law, $N = N_0 \exp(-EW_0{}^2/2\sigma_g^2)$ (Ouchi et al. 2008; Guaita et al. 2010), where w_0 and σ_g are the scale factor and distribution width, respectively. For convenience, we refer to w_0 and σ_g as the scale lengths.

We fitted the distributions with the exponential and Gaussian laws. To fit the data, we take Poisson errors into account. The best-fit w_0 (σ_g) values are $w_0 = 113 \pm 14$ ($\sigma_g = 116 \pm 11$), 68 ± 13 (84 ± 14), and 134 ± 66 Å (148 ± 49 Å) for $z \sim 3.6$, 4.9, and 6.0, respectively[4].

[4] It is not trivial to determine the appropriate number of histogram bins. We applied various bin numbers ranging from 6 to 15. The results are well consistent with each other within uncertainties. The bin number in Fig. 7 is 10.

6.2. Selection cut effects on the distribution of Lyα equivalent widths

Before comparing our scale lengths (w_0 and σ_g) with those in previous studies, we investigated how the values can be affected by the selection of LAEs (i.e., limiting UV magnitudes, Lyα luminosities, and EW_0). Indeed, previous studies have shown that fainter M_{UV} objects have larger EW_0 (e.g., Ando et al. 2006; Ouchi et al. 2008, see also Sect. 7) and that there might be a correlation between $L_{Ly\alpha}$ and EW_0 (Fig. 9 of Gronwall et al. 2007). Thus, the scale lengths may change with different selection cuts, as pointed out by Garel et al. (2015). Because our LAEs span wide ranges of $M_{UV}$and $L_{Ly\alpha}$, we were able to study all of these effects.

To do so, we remeasured EW_0 scale lengths of our LAEs with various selection cuts. As an example, Fig. 8 shows EW_0 scale lengths plotted against various cuts in M_{UV} and $L_{Ly\alpha}$ at $z \sim 3.6$. The left panel of Fig. 8 shows the EW_0 scale lengths for objects satisfying $M_{UV} < M_{UV}$ cut: i.e., we include M_{UV} fainter objects as the M_{UV} cut value increases. We carried out the Spearman rank coefficient test to evaluate the significance of a correlation. In the case of the exponential (Gaussian) law, the rank correlation coefficient is $\rho_{w0} = 0.95$ ($\rho_\sigma = 0.98$), while the probability satisfying the null hypothesis is $p_{w0} = 8.8 \times 10^{-5}$ ($p_\sigma = 1.9 \times 10^{-6}$). Thus, we quantitatively show that including fainter M_{UV} objects increases w_0 and σ_g. A similar relation between EW_0 scale lengths and M_{UV} cuts has been recently demonstrated by Oyarzún et al. (2017) based on a Baysian approach. The right panel of Fig. 8 shows the EW_0 scale lengths for objects satisfying log $L_{Ly\alpha}$ cut < log $L_{Ly\alpha}$: i.e., we include $L_{Ly\alpha}$

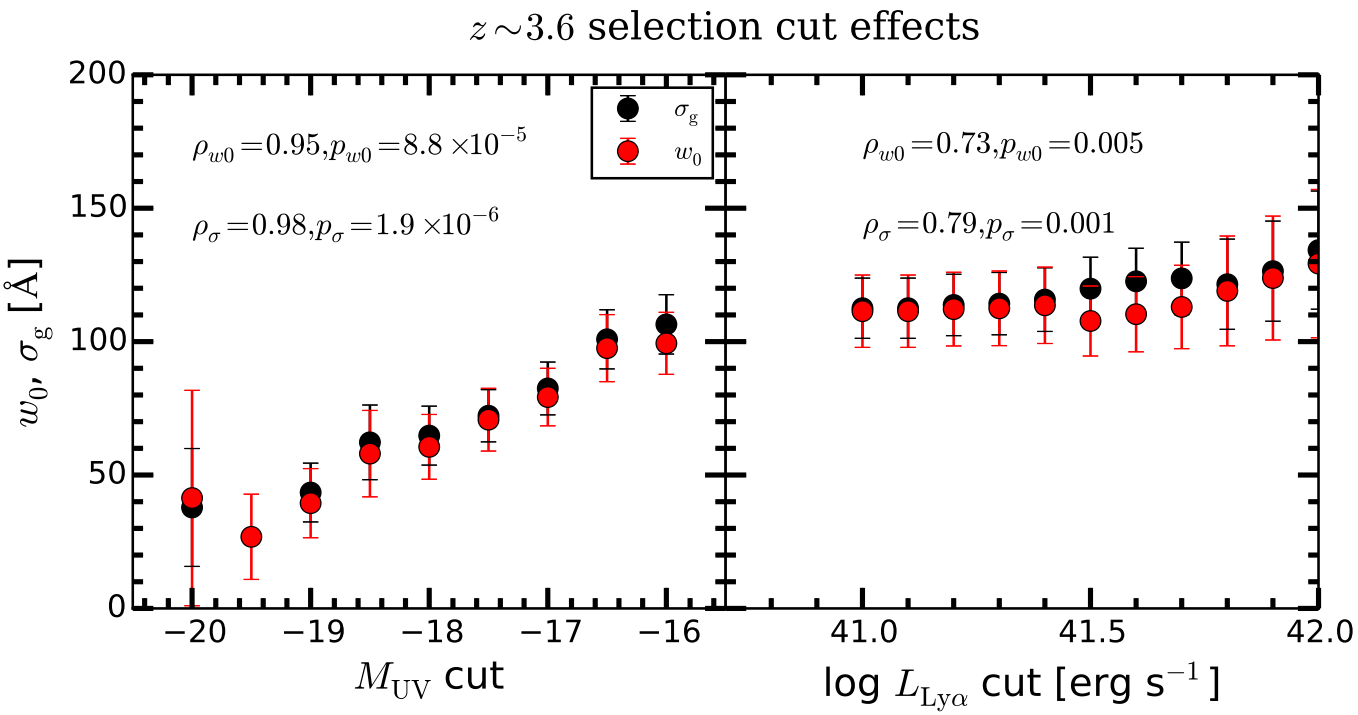


Fig. 8. *From left to right*: w_0 and σ_g for various cuts in M_{UV} and log $L_{Ly\alpha}$ at $z \sim 3.6$. The red and black circles represent the scale factor (w_0) and distribution width (σ_g), respectively. In each panel, ρ_{w0} (ρ_σ) indicates the Spearman rank correlation coefficient for the relation in the case of the exponential (Gaussian) law, while p_{w0} (p_σ) denotes the probability satisfying the null hypothesis.

Table 6. Comparisons of w_0 in this study with those in previous studies with the same selection functions.

Study	Redshift	M_{UV} limit [AB mag]	log $L_{Ly\alpha}$ limit [erg s^{-1}]	Reference w_0 [Å]	w_0 in this study [Å]
(1)	(2)	(3)	(4)	(5)	(6)
$z \sim 3.6$					
Gronwall et al. (2007)	3.1	−18.0	42.0	75 ± 6	74 ± 19
Ciardullo et al. (2012)	3.1	−18.6	42.0	64 ± 9	60 ± 20
$z \sim 4.9$					
Zheng et al. (2014)	4.5	−17.0	42.4	50 ± 11[a] (167^{+44}_{-19})	143 ± 64
$z \sim 6.0$					
Kashikawa et al. (2011)	5.7	−18.0	42.0	108 ± 20[b]	157 ± 110
Kashikawa et al. (2011)	6.6	−18.0	42.0	79 ± 19[b]	157 ± 110

Notes. Comparisons of our w_0 with those in previous studies. For fair comparisons, we apply to our LAEs similar selection cuts adopted in previous studies. (1) Reference study; (2) typical redshift in the reference study; (3) lower limit of M_{UV} in the reference study; (4) lower limit of $L_{Ly\alpha}$ in the reference study; (5) w_0 values in the reference study; and (6) w_0 values in our LAEs with similar selection cuts of (3) and (4). [(a)] The value without parentheses is the scale factor obtained from a direct fitting to the distribution, while the value with parentheses indicates w_0 derived from simulations in Zheng et al. (2014). [(b)] Since the scale factors are not listed in Kashikawa et al. (2011), we take the values from Zheng et al. (2014) who fitted the EW_0 distribution of LAEs in Kashikawa et al. (2011).

faint objects as the log $L_{Ly\alpha}$ cut value decreases. In the case of the exponential (Gaussian) law, the rank correlation coefficient is $\rho_{w0} = 0.73$ ($\rho_\sigma = 0.79$), while the probability satisfying the null hypothesis is $p_{w0} = 0.005$ ($p_\sigma = 0.001$). Although the significance level is weaker than that in the left panel, there is a trend that including fainter $L_{Ly\alpha}$ objects decreases the scale lengths. The correlation is due to the fact that brighter $L_{Ly\alpha}$ objects have larger EW_0 values at a given M_{UV}. For redshift bins at $z \sim 4.9$ and 6.0, we confirmed similar trends between scale lengths and selection cuts.

We now compare the EW_0 scale factor of our LAEs, w_0, with those in previous studies (Gronwall et al. 2007; Ciardullo et al. 2012; Zheng et al. 2014; Kashikawa et al. 2011). For fair comparisons, we applied similar selection cuts as adopted in the previous studies to our LAEs, which are summarized in Table 6. We take the low z case as an example. While the w_0 value for the entire $z \sim 3.6$ sample is 113 ± 14 Å (Fig. 7), the w_0 value significantly reduces to 74 ± 19 Å if we adopt the same selection cut as in Gronwall et al. (2007). The latter value is very consistent with that reported in Gronwall et al. (2007). From this table, we find

that our w_0 values are consistent with those in previous studies within 1σ uncertainties, although these uncertainties are large at $z \sim 4.9$ and 6.0. The results again demonstrate that EW_0 scale lengths are sensitive to the selection functions of LAEs. The results also imply that care must be taken when comparing data points based on different selections.

6.3. Evolution of EW_0 scale lengths

We examined the redshift evolution of the EW_0 scale lengths. For fair comparisons of the scale lengths at different redshifts, we need to take into account the fact that lower z data are deeper than high z data and that the udf-10 field is deeper than the mosaic field in Lyα. To take these into account, we only included LAEs with $M_{\rm UV} < -18.5$ and $\log(L_{{\rm Ly}\alpha}/{\rm erg\ s^{-1}}) > 42.2$ (see black dashed lines in Fig. 6). In these ranges, we are left with 40, 31, and 16LAEs at $z \sim 3.6$, 4.9, and 6.0, respectively. We obtain scale factors of $w_0 = 71 \pm 19$, 81 ± 36, and 107 ± 94 Å at $z \sim 3.6$, 4.9, and 6.0, respectively. Likewise, we obtain distribution widths of $\sigma_{\rm g} = 73 \pm 19$, 87 ± 28, and 148 ± 93 Å at $z \sim 3.6$, 4.9, and 6.0, respectively.

In the top two panels of Fig. 9, we plot the redshift evolution of the scale lengths of our LAEs. The red circles show the redshift evolution for the objects with $M_{\rm UV} < -18.5$ and $(L_{{\rm Ly}\alpha}/{\rm erg\ s^{-1}}) > 42.2$. These scale lengths are apparent values. To correct for IGM attenuation at wavelengths shorter than 1215.67 Å, we used the prescriptions of Inoue et al. (2014), which are updated versions of those of Madau (1995). At $z \sim 3.6$, 4.9, and 6.0, Lyα transmission at wavelengths shorter than 1215.67 Å is 0.51, 0.17, and 0.01, respectively. Correcting our apparent scale lengths with these factors, we obtain intrinsic w_0 ($\sigma_{\rm g}$) values of 94 ± 25 (97 ± 25), 139 ± 62 (149 ± 48), and 212 ± 186 (293 ± 184) Å at $z \sim 3.6$, 4.9, and 6.0, respectively. In the bottom two panels of Fig. 9, the red circles indicate the redshift evolution of the scale lengths corrected for the IGM attenuation on Lyα.

Following Zheng et al. (2014), we evaluated the redshift evolution of the scale lengths in the form of $w_0, \sigma_{\rm g} = A \times (1+z)^{\xi}$, where ξ values indicate the strength of the redshift evolution. In the top two panels, before the IGM correction, we obtain the ξ value of w_0 ($\sigma_{\rm g}$) to be 0.7 ± 1.7 (1.1 ± 1.4). In the bottom two panels, after the IGM correction, we obtain the ξ value of w_0 ($\sigma_{\rm g}$) to be 1.7 ± 1.7 (2.1 ± 1.4). The best-fit curves are shown as black dashed lines in Fig. 9. Owing to the large error bars in the ξ values, we cannot conclude if the redshift evolution of the scale lengths exists. Our ξ values are consistent with the values presented by Zheng et al. (2014) within 1σ uncertainties. Zheng et al. (2014) claimed a strong redshift evolution of scale lengths at $0 < z < 7$ based on a compiled sample of their LAEs and those from the literature. The authors obtained ξ values of w_0 to be 1.1 ± 0.1 (1.7 ± 0.1) before (after) IGM correction. The small uncertainties in ξ values in Zheng et al. (2014) are due to the large number of data points taken from the literature. However, we caution that the compiled sample of Zheng et al. (2014) have complicated selection cuts; the different data points from the literature have different selection cuts. For example, the literature with different selection cuts listed in Table 6 are included in these studies. Therefore, although our ξ values are consistent with those of Zheng et al. (2014) we need a large number of LAEs with a uniform selection function at $0 < z < 7$ for a definitive conclusion (see also Shibuya et al. 2017).

There are two assumptions in the correction of IGM attenuation on Lyα, as discussed in Ouchi et al. (2008). First, the IGM attenuation prescription that we used (Inoue et al. 2014) computes the *mean* Lyα transmission at a given redshift. Observations of $z \sim 2$–3 dropouts show that HI absorption is enhanced near galaxies owing to their biased locations (Rakic et al. 2012; Turner et al. 2014). If the same trend is also true for our LAEs, we may underestimate the effect of IGM attenuation. In this scenario, the true redshift evolution of the intrinsic scale lengths might be stronger than the evolution we show in bottom two panels of Fig. 9. Second, we assumed that the intrinsic Lyα profiles are symmetric around the line center and we applied the IGM attenuation factor to the blue side of the Lyα line only. However, it is well known that the peak of the Lyα line is often redshifted with respect to the systemic redshift (e.g., Steidel et al. 2010; Rakic et al. 2011; Hashimoto et al. 2015; Henry et al. 2015; Inoue et al. 2016; Stark et al. 2017; also Verhamme et al., in prep.), which is often interpreted as a signature Lyα transfer effects in galactic winds. Theoretical studies have shown that the impact of IGM attenuation can be significantly reduced in the case where the Lyα line emerging from galaxies is redshifted by a few hundreds of km s^{-1} (Haiman 2002; Dijkstra et al. 2011; Choudhury et al. 2015; Garel et al. 2012, 2016). Interestingly, Hashimoto et al. (2013), Shibuya et al. (2014), Erb et al. (2014) showed that the Lyα velocity offset is smaller for larger EW_0 objects. Therefore, the true IGM attenuation correction would be larger for larger EW_0 objects. In this case, the true evolution of intrinsic EW_0 scale lengths might be stronger than the evolution we show in bottom two panels of Fig. 9.

To summarize, our data points alone cannot conclude if redshift evolution of the observed EW_0 scale lengths exists. However, IGM correction effects are likely to strengthen the redshift evolution in intrinsic EW_0 scale lengths. We again stress that it is important to take selection function effects into account.

6.4. Assumption of flat β in estimates of EW_0

Many previous studies have assumed flat UV continuum slopes ($\beta = -2.0$) to derive continuum fluxes at 1216 Å (e.g., Malhotra & Rhoads 2002; Shimasaku et al. 2006; Guaita et al. 2011; Mawatari et al. 2012; Zheng et al. 2014; Shibuya et al. 2017). We examine how this assumption affects the redshift evolution of scale lengths. As shown in Table 3, the typical β value is shallower than -2.0 at $z \sim 3.6$. Thus, if we assume a flat β at $z \sim 3.6$, the continuum fluxes at 1216 Å are overestimated, which in turn leads to underestimates of EW_0. In contrast, at $z \sim 4.9$ and 6.0, typical β values are steeper than -2.0 and consequently the EW_0 values are overestimated. These effects therefore naturally lead to underestimates (overestimates) of the scale lengths at $z \sim 3.6$ ($z \sim 4.9$ and 6.0). It is then possible that this can strengthen the redshift evolution of the scale lengths.

To evaluate this, we re-examined the strength of the redshift evolution, ξ, under the assumption of $\beta = -2.0$. Because of the large error bars in ξ values, the results are consistent with those with variable β. Table 7 summarizes the EW_0 statistics and scale lengths for the two cases of variable and fixed β. Although our limited sample does not show the significant impact of the flat β assumption, future works would need to consider variable β to remove possible systematics.

7. Ando effect

We now turn our attention to the relation between EW_0 and $M_{\rm UV}$. As can be seen from Fig. 10, bright continuum objects are always associated with low EW_0 values while UV-faint galaxies span a wide range of EW_0, and some of these galaxies turn out to be

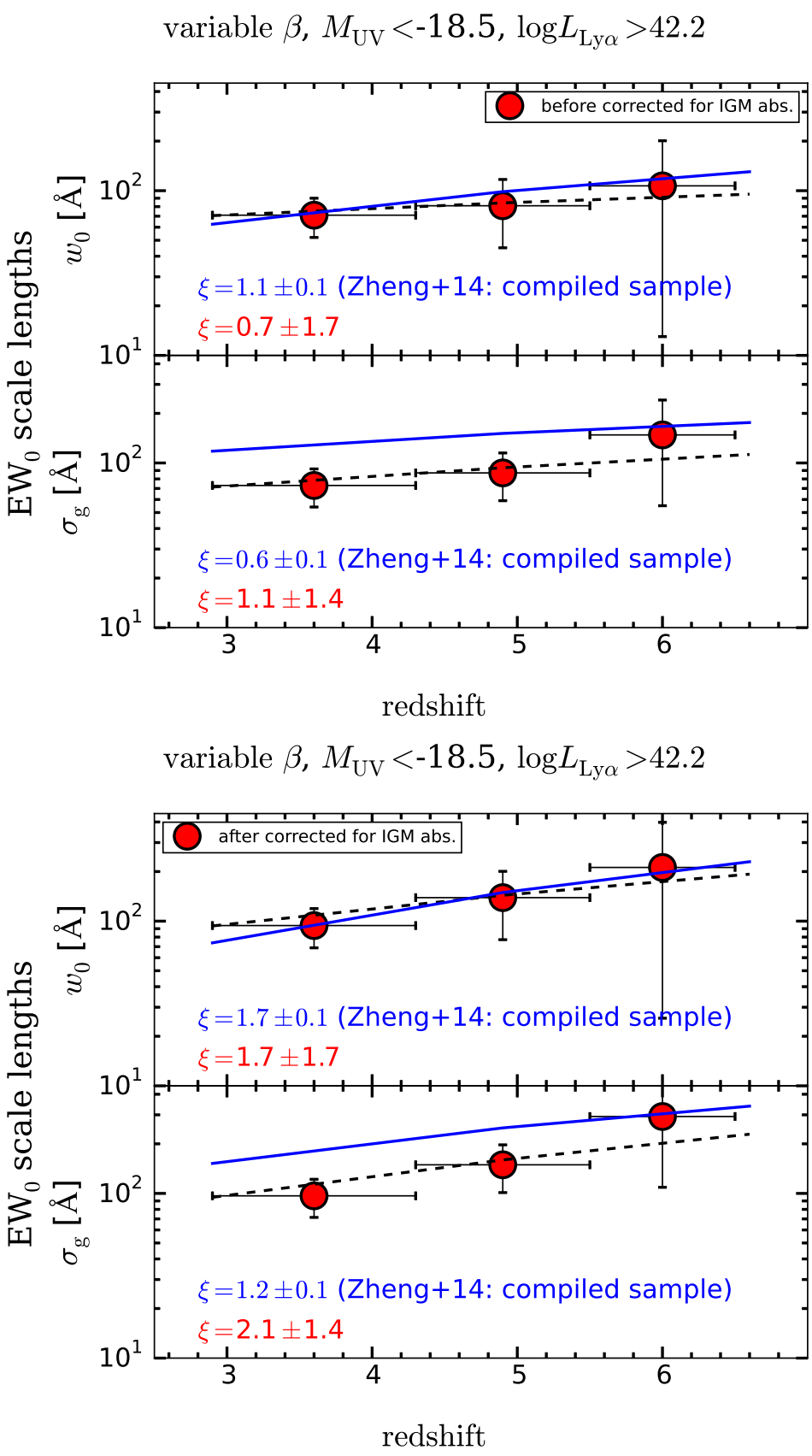


Fig. 9. *Top two panels*: evolution of the scale lengths before the IGM attenuation correction on Lyα. In this study, only LAEs with $M_{\rm UV} < -18.5$ and log $L_{{\rm Ly}\alpha} > 42.2$ are used for fair comparisons at $2.9 < z < 6.6$ (see dashed lines in Fig. 6). The black dashed curves show the best fit to our data points expressed as $A \times (1+z)^{\xi}$, while the blue curves shows the best fit obtained in Zheng et al. (2014) with a compiled sample of LAEs at $0 < z < 7$ that has different selection functions. The ξ value indicates the significance of the redshift evolution of the scale lengths. The *bottom two panels* indicate the evolution of the scale lengths after the IGM attenuation correction on Lyα. Prescriptions of Inoue et al. (2014) were used for the IGM attenuation correction on Lyα. The meanings of the curves are the same as those in the top panels.

Table 7. Summary of the influence of a variable/flat β slope.

Method (1)	Mean EW_0 (2)	Median EW_0 (3)	σ (4)	w_0 (all) (5)	w_0 ($M_{\rm UV} < -18.5$) (6)
$z \sim 3.6$					
variable β	113	87	96	113 ± 14	63 ± 15
flat β	96	79	79	92 ± 11	50 ± 11
$z \sim 4.9$					
variable β	83	56	88	68 ± 13	68 ± 27
flat β	82	60	60	80 ± 17	60 ± 20
$z \sim 6.0$					
variable β	130	97	120	134 ± 66	88 ± 78
flat β	128	76	106	130 ± 67	87 ± 51

Notes. Comparisons of EW_0-related values in two methods: one based on realistic variable β and the other based on the assumption of $\beta = -2.0$. (1) Method; (2) (3) (4) mean, median, and standard deviation of EW_0; (5) scale factors for the entire sample; and (6) scale factors for the limited subsample with $M_{\rm UV} < -18.5$.

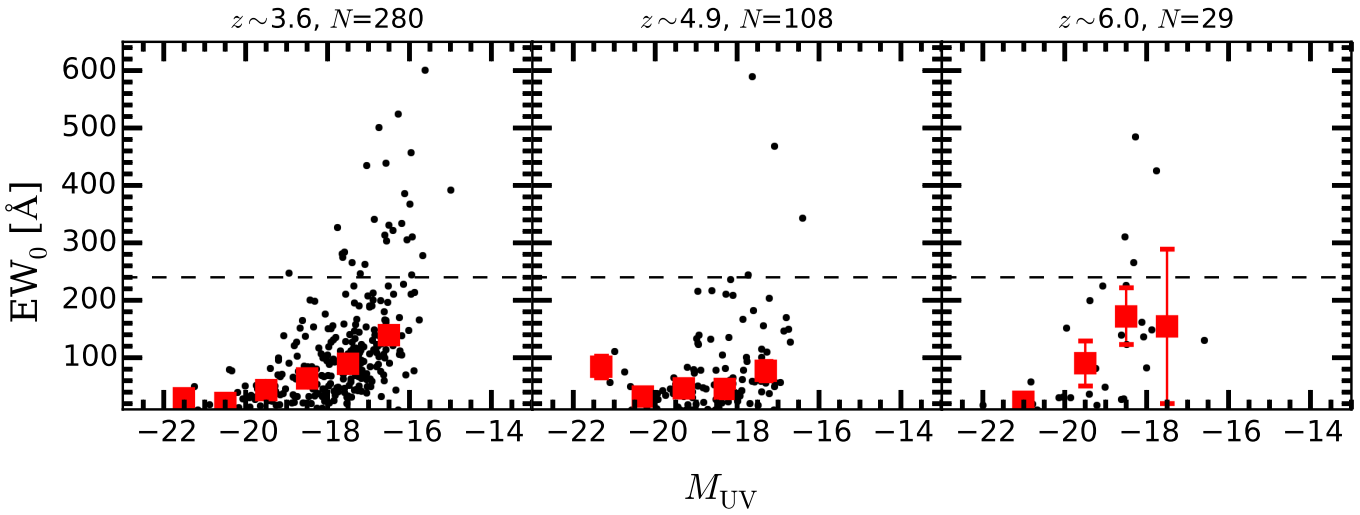


Fig. 10. *From left to right*: EW_0 plotted against $M_{\rm UV}$ for $z \sim 3.6$, 4.9, and 6.0. The black circles indicate our individual LAEs. One (one) objects at $z \sim 3.6$ (4.9) with $EW_0 > 600$ Å are placed at $EW_0 = 600$ Å for display purposes. The horizontal dashed line indicates $EW_0 = 240$ Å (cf. Schaerer 2003; Raiter et al. 2010). The red squares show the biweight mean values of EW_0 in each $M_{\rm UV}$ bin.

very strong emitters. The biweight mean and error values for each magnitude bin are listed in Table 4. This trend was found by Ando et al. (2006) for LBGs at $z \sim 5$–6 and is confirmed by later studies of high z LAEs and LBGs at $z \sim 3$–7 (LAEs: e.g., Shimasaku et al. 2006; Ouchi et al. 2008; Furusawa et al. 2016; Ota et al. 2017; LBGs: e.g., Stark et al. 2010). Following the previous studies, we refer to this effect as the "Ando effect".

While several physical reasons have been invoked to interpret this trend (e.g., Garel et al. 2012; Verhamme et al. 2012), some studies have argued that it can be completely attributed to selection effects. Nilsson et al. (2009) argued that the lack of small EW_0 at faint $M_{\rm UV}$ is due to limiting Lyα values, whereas the lack of large EW_0 at bright $M_{\rm UV}$ is caused by their rarity, i.e., small survey areas (see also Jiang et al. 2013; Zheng et al. 2014).

We examined whether our selection technique generates the Ando effect based on Monte Carlo simulations. We take an example of the result in the low-z bin, $2.90 < z < 4.44$. First, we generated random log $L_{\rm Ly\alpha}$ values that follow the observed Lyα luminosity function in D17. The Lyα luminosity range is set from log $L_{\rm Ly\alpha} = 40.0$ to 44.0 erg s^{-1} with a bin size of log $L_{\rm Ly\alpha} = 0.1$ erg s^{-1}. Based on the results of D17, we assumed log $L^* = 42.59$ erg s^{-1}, log $\phi^* = -2.67$ Mpc^{-3}, and $\alpha = -1.93$, where L^*, ϕ^*, and α represent the characteristic luminosity, characteristic amplitude, and slope of the Schechter function, respectively. Second, we generated random EW_0 values that follow the exponential distribution. We assumed a scale length of $w_0 = 113$ Å based on our results at $2.90 < z < 4.44$ (Fig. 7). Third, we generated random β values that follow a Gaussian distribution with mean and standard deviation values in Table 3. Finally, redshift values are drawn from the uniform random distribution between $2.90 < z < 4.44$. On the assumption that $L_{\rm Ly\alpha}$, EW_0, z, and β do not correlate with each other, we assigned these numbers to each 10 000 mock galaxy. We estimated $M_{\rm UV}$ values in the opposite way as Eqs. (1) to (6). In Fig. 11, the black dots show all 10 000 simulated galaxies. To mimic our observations, we imposed selection cuts of log $L_{\rm Ly\alpha} > 41.0$ and $M_{\rm UV} < -16.0$ on the mock galaxies based on the left panel of Fig. 6. The selected objects are denoted as red circles. As can be seen from Fig. 11, the lower boundary of the relation is created due to the limiting $L_{\rm Ly\alpha}$ value. On the other hand, the upper boundary of the relation is due to the rarity of $M_{\rm UV}$ bright objects with large EW_0 values. These results are consistent with those in, for example, Zheng et al. (2014). Based on these results, we conclude that

Table 8. Properties of 12 very large EW_0 LAEs, $EW_0 > 200$ Å.

ID (1)	z (2)	EW_0 (3)	σ_{200} (4)	log $L_{Ly\alpha}$ (5)	M_{UV} (6)	β (7)	Comment (8)
489	4.16	362 ± 86	1.9	42.2 ± 0.1	−16.8 ± 0.1	−1.5 ± 0.3	
1969	4.08	245 ± 18	2.5	42.9 ± 0.1	−18.9 ± 0.1	−1.9 ± 0.1	
3034	4.26	321 ± 52	2.3	42.5 ± 0.1	−17.8 ± 0.1	−1.4 ± 0.2	
3475	3.16	495 ± 104	2.8	42.3 ± 0.1	−16.7 ± 0.1	−1.7 ± 0.2	
4231	3.47	315 ± 101	1.1	42.1 ± 0.1	−16.6 ± 0.2	−2.1 ± 0.4	
4515	3.66	325 ± 122	1.6	42.0 ± 0.1	−16.4 ± 0.1	−2.1 ± 0.4	
4623	3.55	569 ± 225	1.6	42.2 ± 0.1	−16.2 ± 0.2	−1.6 ± 0.5	
6376	4.29	441 ± 149	1.6	42.3 ± 0.1	−17.0 ± 0.1	−1.3 ± 0.6	
7159	3.00	286 ± 85	1.0	42.4 ± 0.1	−17.6 ± 0.1	−2.1 ± 0.4	Sect. 8.2; weak CIV
7191	3.18	267 ± 67	1.0	42.3 ± 0.1	−17.6 ± 0.1	−1.1 ± 0.3	
7283	3.43	266 ± 60	1.1	42.2 ± 0.1	−17.1 ± 0.1	−2.1 ± 0.3	Sect. 8.3; merger (pair ID = 6923)
4598	5.77	490 ± 199	1.5	42.9 ± 0.1	−18.2 ± 0.2	−1.1 ± 0.6	

Notes. IDs and physical quantities of 12 very large EW_0 LAEs.

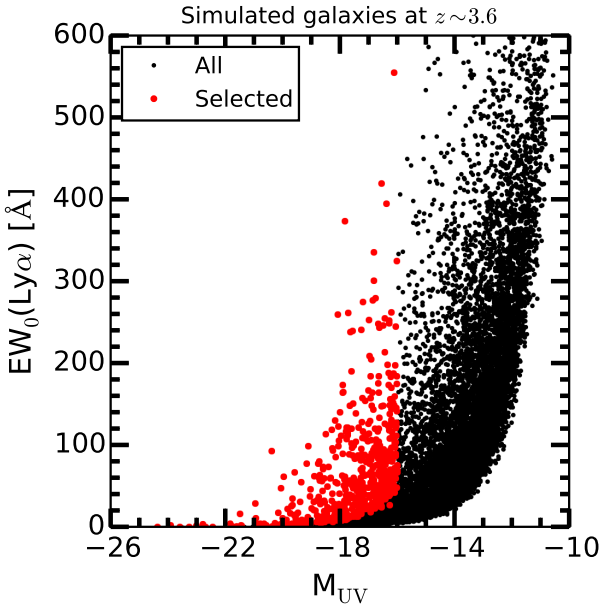


Fig. 11. Lyα equivalent widths plotted against M_{UV} for simulated objects $z \sim 3.6$. The black dots show all mock galaxies with a limiting Lyα luminosity of log $L_{Ly\alpha} = 40.0$. The red circles indicate mock galaxies after the selection cuts of $M_{UV} < -16.0$ and log $L_{Ly\alpha} > 41.0$ to mimic our observations.

we cannot rule out the possibility that the Ando effect is completely due to the selection bias if our assumptions are correct.

8. Very large Lyα equivalent width Lyα emitters

8.1. 12 Very large Lyα equivalent width Lyα emitters

Very large EW_0 LAEs are interesting because they are candidates for galaxies in the early stages of the galaxy formation and evolution (Hashimoto et al. 2017, and references therein). In this study, we define very large EW_0 LAEs as objects having $EW_0 > 200$ Å. We list 12 LAEs with $EW_0 > 200$ Å above 1σ uncertainties in Table 8. To investigate the significance, we calculated $\sigma_{200} = (EW_0 - 200)/EW_{0\mathrm{err.}}$, where $EW_{0\mathrm{err.}}$ is the error value of EW_0. The values range from $\sigma_{200} = 1.0$ to 2.8.

We compared our σ_{200} with those in previous studies that focus on properties of very large EW_0 LAEs. Kashikawa et al. (2012) reported a spectroscopically identified very large EW_0 LAE at $z = 6.5$. The object has $EW_0 = 436^{+422}_{-149}$ Å[5], corresponding to $\sigma_{200} = 1.6$. Sobral et al. (2015) reported a very bright LAE at $z = 6.6$, CR7, whose Lyα is spectroscopically identified. This object has $EW_0 = 211 \pm 20$ Å, corresponding to $\sigma_{200} = 0.6$. Recently, Hashimoto et al. (2017) have investigated six $z \sim 2$ LAEs with very large EW_0. In this study, four objects have $EW_0 > 200$ Å with $\sigma_{200} = 0.7$–5.3. Therefore, our σ_{200} are similar to those in previous studies that focus on very large EW_0 LAEs. Among the 12 very large EW_0 LAEs, four objects, ID 3475, ID 4623, ID 6376, and ID 4598, have extremely large $EW_0 \gtrsim 400$–600 Å. In these objects, EW_0 and σ_{200} values are comparable to or higher than the very large EW_0 LAE studied by Kashikawa et al. (2012).

Also, our very large EW_0 LAEs have relatively shallow β values, -1.6 ± 0.1, where uncertainty denotes the standard error. The result can indicate the presence of nebular continuum (Schaerer 2003). Alternatively, these red β values can also indicate that our LAEs are affected by hidden AGN activity.

In the following sections, we investigate two very large EW_0 LAEs whose EW_0 can be explained by mergers or hidden type-II AGN activity. We discuss possible explanations for the remaining 10 very large EW_0 LAEs in Sect. 9.2.

8.2. ID 7159: Detection of CIV λ1549 – an AGN-like Lyα emitter?

Object ID 7159, at $z = 3.00$, has $M_{UV} = -17.6 \pm 0.1$ and $EW_0 = 286 \pm 85$ Å. The object has a detection of the CIV λ1549 line, but does not have detections of the CIII] λ1908 nor HeII λ1640 lines. Since the CIV line is often associated with AGN activity, it is possible that hidden AGN activity produces additional ionizing photons (e.g., Malhotra & Rhoads 2002; Dawson et al. 2004). However, Stark et al. (2015) revealed that the CIV line can also be emitted by a young stellar population with very hot metal-poor stars (see also Christensen et al. 2012; Mainali et al. 2017; Schmidt et al. 2017). Indeed, ID 7159 has Lyα FWHM of 464 km s^{-1} after the instrumental correction, which is similar to the typical FWHM value of $z \sim 2$–3 LAEs, 100–500 km s^{-1} (e.g., Trainor et al. 2015; Hashimoto et al. 2017). Therefore, it is

[5] The value given in Kashikawa et al. (2012), $EW = 872^{+844}_{-298}$ Å, is after the correction for the IGM attenuation on Lyα. For a fair comparison with our values, we used the EW_0 before the correction for IGM attenuation.

difficult to conclude whether ID 7159 is a star-forming LAE or an AGN-like LAE with the current data[6].

8.3. ID 7283: Merger activity?

Interestingly, we found that one of the 12 very large EW_0 LAEs, ID 7283, has a companion LAE, ID 6923, at a similar redshift. The projected distance between the pair is ∼25 kpc. Based on the Lyα narrowband image, we confirmed that Lyα emission of the pair LAEs are well separated and not contaminated by the Lyα emission of the companion.

It is possible that Lyα emission in the pair LAEs is powered by collisional excitation followed by merger activity and subsequent gravitational cooling (e.g., Taniguchi & Shioya 2000; Otí-Floranes et al. 2012; Rosdahl & Blaizot 2012). Alternatively, the pair might create strong ionizing fields that serve as external UV background sources for each object, leading to additional fluorescent Lyα emission from circum-galactic gas.

9. Discussion

9.1. Limitations of this study

In this study, we excluded (1) 78 objects with spatially multiple HST counterparts. Hereafter we refer to these objects as blended LAEs. The procedure is needed to construct a clean sample in which EW_0 values are robustly measured. For example, if we mistakenly allocated our MUSE Lyα emission to an HST counterpart, the EW_0 values would be incorrect as well. In addition, we excluded (2) 176 objects with a spatially single HST counterpart, but which do not have enough (to be defined) multicolor images. Hereafter, we refer to these objects as very UV faint LAEs. This procedure is also needed to derive EW_0 values with small systematic uncertainties introduced by the flat β ($\beta = -2.0$) assumption. However, since the number fraction of theses LAEs are not negligible (11% and 26%), we discuss possible bias effects introduce by excluding these objects (see Sect. 2.4.2).

To examine the first point, we compared Lyα fluxes of the two samples: blended LAEs and non-blended LAEs. To do so, we performed a two-sample K-S test. We find that the p-value is 0.0001, indicating that the Lyα flux distributions of the two samples are statistically different with each other. Likewise, we compared HST magnitudes of the two samples based on a K-S test. In this analysis, we used HST magnitudes of the nearest counterpart. We take F775W, F105W, and F125W as examples. We find that the p-values are <0.0001 in these HST wave bands, indicating that the HST magnitude distributions of the two samples are statistically different. These results suggest that excluding blended LAEs can introduce a bias effect in terms of Lyα fluxes and HST magnitudes (thus $M_{\rm UV}$). More specifically, we find that Lyα fluxes and HST magnitudes are brighter in blended LAEs than in non-blended LAEs. Because we cannot allocate our MUSE Lyα emission to one of the HST counterparts in these cases, we cannot obtain accurate EW_0 measurements. Under the assumption that the brightest HST counterpart is responsible for the MUSE Lyα emission, we could obtain lower limits of EW_0. We leave these analyses to future works and stress that possible bias effects can change our results. Nevertheless, we can discuss the blending effects because of the high spatial resolution of HST. For example, observations based on ground telescopes alone cannot easily investigate these effects due to their limited spatial resolutions. In this sense, these results are our current best efforts.

We also examine the second point, very faint UV LAEs. Because these very faint UV objects would have very large EW_0 values (or at least very large lower limits of EW_0 values given the Ando effect), the actual EW_0 distributions can be different from what we show in Fig. 7. In our discussion, the redshift evolution of EW_0 scale lengths can be affected by this effect. However, as we described in Sect. 6.3, as long as we use sufficiently bright objects, our discussion remains unchanged. The detailed properties of these very faint UV LAEs will presented in Maseda et al. (in prep.).

9.2. Lyα emission powered by star formation

The EW_0 value encapsulates valuable information about galaxies because this value is the ratio of the Lyα emission and stellar continuum. This value is however a complex quantity hard to interpret because its strength is determined by several aspects that cannot be disentangled easily. Hereafter, we discuss our results in the light of previous studies on EW_0 at high redshift with a particular focus on the comparison with theoretical predictions.

In parallel to high-redshift galaxy surveys, much progress has been made over the last few years to reconcile observational constraints on LBGs and LAEs with theoretical predictions. Under the assumption that Lyα photons result from hydrogen recombination in star-forming regions, the observed Lyα and UV luminosity functions at $3 < z < 6$ can be reproduced by various cosmological hydrodynamical simulations and semi-analytic models, at least within the observational uncertainties (e.g., Dayal et al. 2008; Orsi et al. 2012; Garel et al. 2015). However, these simulations often fail at reproducing quantitatively the global shape of the EW_0 distribution. Unlike the observed distributions that usually peak at a lower EW_0 limit (which depends on the LAE selection) and extend to ≳200 Å, models often predict much narrower distributions and struggle to recover the high fraction of objects with moderately large EW_0, 100−200 Å, (Dayal et al. 2008; Garel et al. 2012). Below, we discuss possible mechanisms to reproduce a higher fraction of moderately large EW_0 LAEs.

It has been shown that assuming different IMFs mostly changes the peak value of the EW_0 distribution but does not increase its width (e.g., Garel et al. 2015), unless one adopts evolving or spatially varying IMFs within galaxies (e.g., Orsi et al. 2012). Nevertheless, at fixed IMF, Forero-Romero & Dijkstra (2013) hinted that the stochastic sampling of the IMF can induce fluctuations in the predicted EW_0 values for a given star formation event, hence broadening the EW_0 distributions (see also Mas-Ribas et al. 2016). Alternatively, bursty star formation may also help reconcile models and observations. Garel et al. (2015) showed that bursty star formation can be more likely to be achieved if one increases the gas surface density threshold to trigger the formation of stars. This can in turn give rise to Lyα-bright and Lyα-quiescent phases. Then, at a given time, galaxies exhibit a wide range of EW_0 values between 0 and ≈200 Å, which depends on the time delay since the last starburst; these values are in better agreement with our observations.

In addition to the problem of moderately large EW_0 LAEs discussed above, we demonstrated that 12 LAEs in our sample have EW_0 values larger than the typical maximal value predicted by stellar synthesis models based on standard IMFs and solar metallicity ($EW_{\rm max} \approx 240$ Å; see red curves in Fig. 12). While

[6] The X-ray flux upper limits of ID 7159 are 1.9×10^{-17}, 6.4×10^{-18}, and 2.7×10^{-17} erg cm^{-2} s^{-1} in the three bands at 0.5−7.0 keV, 0.5−2.0 keV, and 2−7 keV, respectively (see Sect. 5).

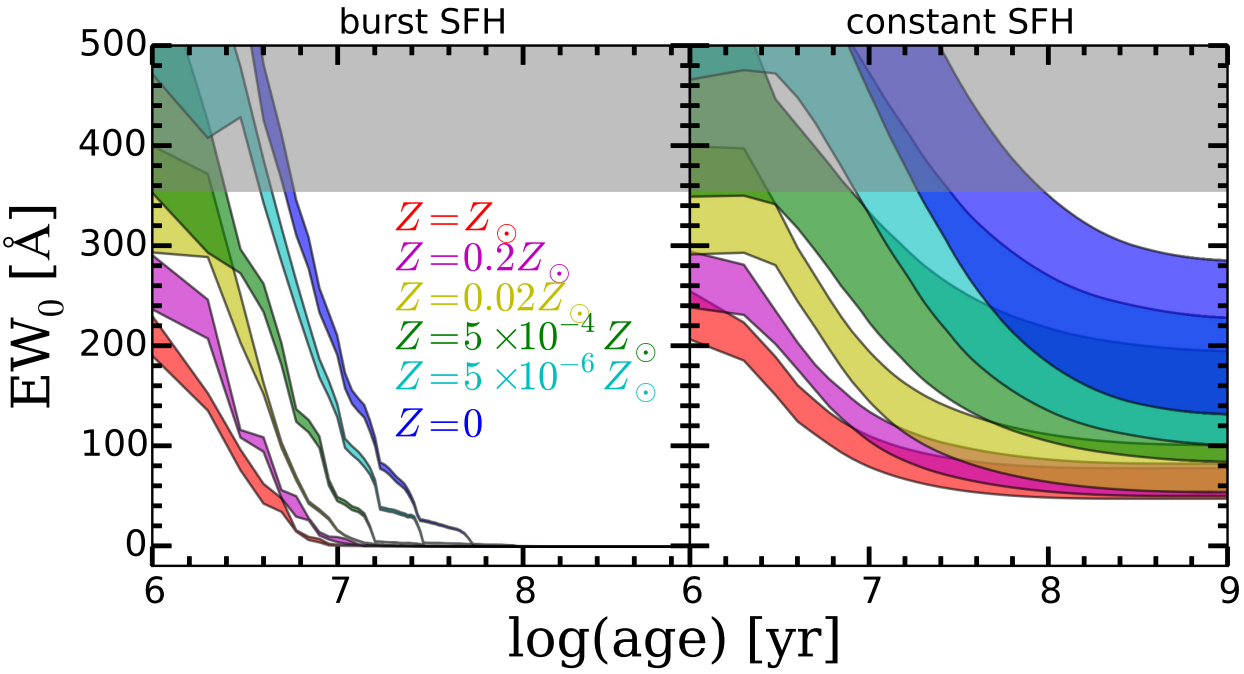


Fig. 12. Comparisons of the observational constraints on EW_0 with the models of Schaerer (2003), Raiter et al. (2010). These models show evolution of the spectral properties of stellar populations for stellar ages varying from 10^4 yr to 1 Gyr for the starburst SFH (*left panel*) and the constant SFH (*right panel*). Different colors correspond to six metallicities: Z = 0 (PopIII, blue), 5×10^{-6} $Z_\odot$ (cyan), 5×10^{-4} $Z_\odot$ (green), 0.02 $Z_\odot$ (yellow), 0.2 $Z_\odot$ (magenta), and $Z_\odot$ (red). For each metallicity, the colored shaded regions denote EW_0 ranges traced by the three three power-law IMFs: two Salpeter IMFs (1−100 $M_\odot$ and 1−500 $M_\odot$) and a Scalo IMF (1−100 $M_\odot$). The horizontal gray shaded regions indicate the range of nine very large EW_0 LAEs without signatures of mergers or AGNs.

two of the 12 very large EW_0 LAEs might be AGNs or mergers (Sect. 8), other interpretations are required for the 10 remaining LAEs with very large EW_0 values. To discuss these very large EW_0 LAEs, we follow the procedure in Hashimoto et al. (2017) who have used the models of Schaerer (2003) and its updated version by Raiter et al. (2010) to constrain the properties of very large EW_0 LAEs. These models cover metallicities from Pop III to solar and a wide range of IMFs assuming two different star formation histories (SFH): an instantaneous burst (starburst SFH) and constant star formation (constant SFH). Given that large EW_0 LAEs have low metallicities, these models with fine low-metallicity grids are very appropriate to investigate the large EW_0 LAEs.

Figure 12 shows the predicted EW_0 value as a function of age, where each curve corresponds to the EW_0 evolution for a given stellar metallicity and the colored shaded regions represent the range spanned by the three assumed IMFs. We see that higher EW_0 values are expected for younger stellar ages and lower metallicities for both the starburst (left panel) and the constant SFH (right panel). In the case of a starburst, the timescale for the Lyα line to be visible reflects the lifetime of O-type stars, and increases toward lower metallicities, reaching log(age yr^{-1}) $\approx$ 7.5 for PopIII stars. For a constant SFH, the EW_0 values decrease over similar (though slightly longer) timescales and then settle into a nearly constant regime with the EW_0 value ranging from $\approx$50 Å for solar metallicity to $\approx$300 Å for zero metallicity. The gray shaded regions in Fig. 12 depict the range spanned by our 10 LAEs. The mean and standard error values of this subsample is 389 ± 36 Å, and here, we adopt the 1σ lower limit, 353 Å. The comparison with the model predictions shows that our very large EW_0 LAEs can be explained by a recent burst of star formation ($\approx$10 Myr) with $Z \lesssim 0.02\ Z\odot$, or by a stellar population younger than $\approx$100 Myr (also with $Z \lesssim 0.02\ Z\odot$) for a constant SFH[7].

While these quantities are hard to constrain observationally, predictions from hydrodynamical simulations suggest that galaxies can exhibit lower stellar metallicities at higher redshift (Ma et al. 2016; Taylor & Kobayashi 2016). In addition, our largest EW_0 values correspond to faint galaxies ($M_{\rm UV} \gtrsim -18$), which plausibly consist of low-mass objects. According to simulations, less massive galaxies tend to have more bursty SFH and lower stellar metallicity at a given redshift (Ma et al. 2016; Sparre et al. 2017). Interestingly, Sparre et al. (2017) show that low-mass galaxies ($\lesssim 10^9$ $M_\odot$) form most their stars during intense bursts of star formation, whereas the time fraction spent in burst cycles (i.e., the *duty cycle*) is about 10−20% at all masses. This *duty cycle* can be compared with the fraction of very strong emitters ($EW_0 \geq 200$ Å) among faint galaxies in our sample ($\approx$250 galaxies with $M_{\rm UV} \gtrsim -18$): $\approx$5% for objects with EW_0 uncertainties above 1σ, and $\approx$13% otherwise. Overall, bursty star formation associated with subsolar metallicities seem able to account for the observed EW_0 distribution, in particular the very large EW_0. Nonetheless, in the next sections, we investigate alternative interpretations of the very large EW_0 values of the nine LAEs without signatures of mergers or AGNs.

[7] Hashimoto et al. (2017) have also used β values to place constraints on stellar ages and metallicities. To use β, we need to correct these values with dust extinction effects. Currently, dust extinction values, $E(B-V)$, are not available for our LAEs. Thus, we assume that that our intrinsic β values are bluer than those in Table 8. We find that our relatively shallow mean β value, −1.6 ± 0.1, does not tighten the ranges of the stellar age and metallicity of our very large EW_0 LAEs.

9.3. Radiative transfer and EW_0 boost

When propagating through inhomogeneous or multiphase media, Lyα photons often take a very different path compared to non-resonant continuum photons. Under given conditions, the Lyα escape fraction can then become larger than the UV continuum escape fraction, hence boosting the observed EW_0. For instance, in the clumpy ISM model in which dust is locked into HI clouds (Neufeld 1991; Hansen & Oh 2006), Lyα photons scatter off the surface of the clouds while continuum radiation can penetrate the clouds and be absorbed by dust grains. This scenario has notably been shown to well recover the EW_0 distributions along with the luminosity functions, when brought into the cosmological context using cosmological simulations or semi-analytic models (Kobayashi et al. 2010; Shimizu et al. 2011). Some numerical Lyα transfer experiments have claimed that a significant boost of the *angular-average* EW_0 can only be achieved under physical conditions, such as metallicity, gas density, velocity, and covering fraction, which are unlikely to be representative of the ISM at high redshift (Laursen et al. 2013; Duval et al. 2014). Similarly, Gronke & Dijkstra (2014) investigated the angular variation of the EW_0 and they concluded that this quantity can be strongly enhanced along a limited number of sight lines.

Similarly, the escape of Lyα photons is found to be highly anisotropic for non-spherical gas distribution (e.g., discs, bipolar winds; Verhamme et al. 2012; Behrens et al. 2014; Zheng & Wallace 2014) and varies as a function of the inclination angle. Even in the case where the global (i.e., angle average) Lyα escape fraction remains lower than that of UV photons because of Lyα resonant scattering, Lyα photons may preferentially emerge from galaxies along low HI-opacity sight lines, increasing the EW_0 in these directions. Quantitatively speaking, these simulations predict that the EW_0 can be boosted up to a factor of $\approx$3, depending on the exact geometry, HI density, and velocity fields or the amount of dust. Although radiative transfer effects undoubtedly play a role in shaping the Lyα emission properties of high-redshift galaxies, it remains difficult to determine at which extent these are responsible for the very large EW_0 that we observe.

9.4. Other Lyα production channels

The very large EW_0 values observed in our sample may also indicate objects for which a significant fraction of Lyα radiation is not produced by internal star formation. For example, by observing around a bright quasar, Cantalupo et al. (2012) found a large sample of very large EW_0 LAEs for which the Lyα emission is most likely powered by fluorescence from the quasar illumination, up to a few hundred comoving Mpc^3 around the quasar (see also Borisova et al. 2016a; Marino et al. 2017). To investigate this issue, we searched for quasars in and around the UDF using the Veron Cetty catalog[8]. We used the large search radius of 10 arcmin from the center position of the UDF. We find that there are no nearby QSOs within 10 comoving Mpc from our very large EW_0 LAEs. The result indicates that there are no detectable active QSOs in current catalogs that can contribute to increasing the EW_0 value of our very large EW_0 sources with fluorescence. However, because of light travel effects, we cannot exclude the possibility that past QSO phases in neighboring galaxies within a few Mpc from our very large EW_0 LAEs could be responsible for the Lyα boosting, especially if QSO phases are short but relatively frequent (e.g., Cantalupo et al. 2007, 2012; Trainor & Steidel 2013; Borisova et al. 2016b; Marino et al. 2017). In particular, if all our very large EW_0 values are due to this effect, this could give us potential constraints on the AGN phase duty cycle. We will investigate this in detail in future work.

Likewise, it is possible that nearby AGN activity contributes to Lyα fluorescence. For the 10 large EW_0 LAEs without signatures of mergers or AGN activity, we found that none of these objects have nearby AGNs (Luo et al. 2017) within 10 comoving Mpc. Therefore, it is unlikely that AGN Lyα fluorescence contribute to the very large EW_0 values, although hidden type-II AGN activity might do the job.

Another source of Lyα emission, independent of star formation, is gravitational cooling radiation. This mechanism has been invoked to explain giant Lyman-alpha blobs (see, e.g., Haiman et al. 2000; Fardal et al. 2001; Dijkstra & Loeb 2009). There exist theoretical and numerical quantitative predictions for this process, although large uncertainties remain. These predictions suggest that a luminosity of $(L_{\mathrm{Ly}\alpha}/\mathrm{erg\ s^{-1}}) \sim 10^{42}$ erg s^{-1} can be produced by gas falling into a dark matter (DM) halo with a mass of $M_{\mathrm{h}} \sim 3 \times 10^{11}\ M_{\odot}$ (Dijkstra & Loeb 2009; Faucher-Giguère et al. 2010; Rosdahl & Blaizot 2012; Yajima et al. 2012). From Table 8, we see that this can easily account for half the flux of most of our very large EW_0 objects. Therefore, gravitational mechanism would explain an EW_0 twice as large as star formation would allow. If this is the case, we do need neither extremely young stellar age nor low metallicity to explain very large EW_0 objects. The two brightest objects of Table 8 (ID = 1969 and 4598) have a luminosity almost an order of magnitude larger. If they are in a DM halo of mass of $M_{\mathrm{h}} \sim 3 \times 10^{11}\ M_{\odot}$, cooling radiation may only boost their EW_0 by $\sim$10%. This is not quite enough to reconcile them with the star formation limit. Nevertheless, the quasi-linear relation between $L_{\mathrm{Ly}\alpha}$ and M_{h} for cooling radiation implies that only a moderately larger DM halo host would be able to do the job.

10. Summary and conclusions

We have presented a new large data set of 417 LAEs detected with MUSE at $2.9 < z < 6.6$ in the *Hubble* Ultra Deep Field (UDF). Owing to the high sensitivity of MUSE, we detected Lyα emission from $\log\ (L_{\mathrm{Ly}\alpha}/\mathrm{erg\ s^{-1}}) \sim 41.0$ to 43.0. For the estimates of Lyα fluxes, we adopted the curve of growth technique to capture the extended emission. Taking into account the extended Lyα emission is important for accurate measurements of EW_0 because a significant fraction of Lyα emission originates from the extended component, the so-called Lyα halo (see L17). In addition, with deep HST photometry data in the UDF, we derived UV slopes (β) and continuum fluxes of our LAEs. The UV absolute magnitudes range from $M_{\mathrm{UV}} \sim -16.0$ to -21.0 ($0.01-1.0\ L^*_{z=3}$). The faint-end $L_{\mathrm{Ly}\alpha}$ and M_{UV} values at $z \sim 3.6$ and 4.9 are roughly one order of magnitude fainter than those in previous LAE studies based on the narrowband technique (Fig. 6). We derived EW_0 values and focused on two controversial issues: first, the evolution of the EW_0 distribution between $z = 2.9$ and 6.6, and second, the existence of very large EW_0 LAEs. Our main results are as follows:

– The median β values in our LAEs are -1.73 ± 0.04, -2.22 ± 0.15, and -2.31 ± 0.19 at $z \sim 3.6$, 4.9, and 6.0, respectively, where error values denote the standard errors. The high dynamic range of M_{UV} in our LAEs allows us to investigate β values in as much detail as those in dropout galaxies. We

[8] https://heasarc.gsfc.nasa.gov/db-perl/W3Browse/

find a trend that β becomes steeper at faint $M_{\rm UV}$. The slope $d\beta/dM_{\rm UV}$ of our LAEs is in good agreement with that in dropout galaxies, ≈ -0.1 (Sect. 3.2 and Figs. 2 and 3). We also find that β becomes steeper at high z. At both bright ($M_{\rm UV} \approx -19.5$) and faint ($M_{\rm UV} \sim -17.5$) UV magnitude bins, the typical β values decrease from ≈ -1.8 to -2.5 at $z \sim 3.6$ and 6.0, respectively, which is consistent with results for dropout galaxies (Sect. 3.3 and Fig. 4). These results imply that our LAEs have lower dust contents or younger stellar populations at higher z and fainter $M_{\rm UV}$.

– The EW_0 values span the range of $\approx$5 to 240 Å or larger, and the EW_0 distribution can be well fitted by the exponential law, $N = N_0 \exp(-EW_0/w_0)$ (Sect. 6.1 and Fig. 7). We find that a fainter limiting $M_{\rm UV}$ cut increases w_0 (Sect. 6.2 and Fig. 8). These results indicate that selection functions affect w_0, and care must be taken for the interpretation of the EW_0 distribution, its redshift evolution, and their comparisons with previous works. Taking these effects into account, we find that our w_0 values are consistent with those in the literature within 1σ uncertainties at $2.9 < z < 6.6$ at a given $M_{\rm UV}$ threshold (Sect. 6.3 and Fig. 9). Given large error bars in our w_0 values, our data points alone cannot conclude if there exits a redshift evolution of w_0. We need a large sample of LAEs for a definitive conclusion.
– We presented 12 LAEs with $EW_0 > 200$ Å above 1σ uncertainties (Sect. 8, Table 8). Among these objects, two LAEs have signatures of merger or AGN activity indicating that part of the Lyα emission is contributed from non-star-forming activity. For the remaining 10 LAEs without signatures of mergers or AGNs, we constrain stellar ages and metallicities based on comparisons between observed EW_0 values with stellar synthesis models of Schaerer (2003) and Raiter et al. (2010) under the assumption that all the Lyα emission originates from star-forming activity. We find that these very large EW_0 can be reproduced by a recent burst of star formation ($\approx$10 Myr) with $Z \lesssim 0.02\ Z_\odot$, or by a stellar population younger than $\approx$100 Myr (also with $Z \lesssim 0.02\ Z_\odot$) for a constant star formation history. To put it in another way, the very large EW_0 values can be explained without invoking PopIII stars or extremely top-heavy IMFs. Alternatively, these very large EW_0 can be also explained by, for example, anisotropic radiative transfer effects, fluorescence by hidden AGN or QSO activity, and/or gravitational cooling.

These possible scenarios for very large EW_0 LAEs are also invoked to explain Lyα halo properties presented in L17. Thus, in conjunction with our EW_0 and Lyα halo properties (L17), future Hα emission line observations with, for example, MOSFIRE on Keck and The *James Webb* Space Telescope (JWST), will be very useful to put tighter constraints on these scenarios (L17, Cantalupo 2017; Mas-Ribas et al. 2017).

Acknowledgements. This research has been produced within the FOGHAR ANR project ANR-13-BS05-110 and the Labex LIO (Lyon Institute of Origins) of the Programme Investissements d'Avenir ANR-10-LABX-66. T.H. acknowledges the JSPS Research Fellowship for Young Scientists. T.G. is grateful to the LABEX Lyon Institute of Origins (ANR-10-LABX-0066) of the Université de Lyon for its financial support within the program "d'Avenir" (ANR-11-IDEX-0007) of the French government operated by the National Research Agency (ANR). J.R. acknowledges support from the ERC starting grant 336736-CALENDS. J.S. thanks the ERC Grant agreement 278594-GasAroundGalaxies. R.A.M. acknowledges support by the Swiss National Science Foundation. J.B. acknowledges support by Fundação para a Ciência e a Tecnologia (FCT) through national funds (UID/FIS/04434/2013) and Investigador FCT contract IF/01654/2014/CP1215/CT0003, and by FEDER through COMPETE2020 (POCI-01-0145-FEDER-007672). S.C. gratefully acknowledges support from Swiss National Science Foundation grant PP00P2_163824. We acknowledge Akio K. Inoue for providing us with the results of his Lyα transmission shortward of the line. We are grateful to Nobunari Kashikawa and Zhenya Zheng for providing us with their data. We thank Masami Ouchi, Yuichi Matsuda, Takatoshi Shibuya, Ken Mawatari, and Kohei Ichikawa for useful discussions.

References

Adams, J. J., Blanc, G. A., Hill, G. J., et al. 2011, ApJS, 192, 5
Akhlaghi, M., & Ichikawa, T. 2015, ApJS, 220, 1
Ando, M., Ohta, K., Iwata, I., et al. 2006, ApJ, 645, L9
Bacon, R., Accardo, M., Adjali, L., et al. 2010, in Ground-based and Airborne Instrumentation for Astronomy III, Proc. SPIE, 7735, 773508
Bacon, R., Brinchmann, J., Richard, J., et al. 2015, A&A, 575, A75
Bacon, R., Conseil, D., Mary, D., et al. 2017, A&A, 608, A1 (MUSE UDF SI, Paper I)
Beckwith, S. V. W., Stiavelli, M., Koekemoer, A. M., et al. 2006, AJ, 132, 1729
Behrens, C., Dijkstra, M., & Niemeyer, J. C. 2014, A&A, 563, A77
Blanc, G. A., Adams, J. J., Gebhardt, K., et al. 2011, ApJ, 736, 31
Borisova, E., Cantalupo, S., Lilly, S. J., et al. 2016a, ApJ, 831, 39
Borisova, E., Lilly, S. J., Cantalupo, S., et al. 2016b, ApJ, 830, 120
Bouwens, R. J., Illingworth, G. D., Franx, M., et al. 2009, ApJ, 705, 936
Bouwens, R. J., Illingworth, G. D., Oesch, P. A., et al. 2011, ApJ, 737, 90
Bouwens, R. J., Illingworth, G. D., Oesch, P. A., et al. 2012, ApJ, 754, 83
Bouwens, R. J., Illingworth, G. D., Oesch, P. A., et al. 2014, ApJ, 793, 115
Brinchmann, J., Inami, H., Bacon, R., et al. 2017, A&A, 608, A3 (MUSE UDF SI, Paper III)
Cantalupo, S. 2017, in Astrophys. Space Sci. Lib. 430, eds. A. Fox, & R. Davé, 195
Cantalupo, S., Lilly, S. J., & Porciani, C. 2007, ApJ, 657, 135
Cantalupo, S., Lilly, S. J., & Haehnelt, M. G. 2012, MNRAS, 425, 1992
Cassata, P., Tasca, L. A. M., Le Fèvre, O., et al. 2015, A&A, 573, A24
Charlot, S., & Fall, S. M. 1993, ApJ, 415, 580
Choudhury, T. R., Puchwein, E., Haehnelt, M. G., & Bolton, J. S. 2015, MNRAS, 452, 261
Christensen, L., Laursen, P., Richard, J., et al. 2012, MNRAS, 427, 1973
Ciardullo, R., Gronwall, C., Wolf, C., et al. 2012, ApJ, 744, 110
Cowie, L. L., & Hu, E. M. 1998, AJ, 115, 1319
Cowie, L. L., Barger, A. J., & Hu, E. M. 2011, ApJ, 738, 136
Dawson, S., Rhoads, J. E., Malhotra, S., et al. 2004, ApJ, 617, 707
Dayal, P., Ferrara, A., & Gallerani, S. 2008, MNRAS, 389, 1683
Dijkstra, M. 2014, PASA, 31, e040
Dijkstra, M., & Loeb, A. 2009, MNRAS, 396, 377
Dijkstra, M., Haiman, Z., & Spaans, M. 2006, ApJ, 649, 14
Dijkstra, M., Mesinger, A., & Wyithe, J. S. B. 2011, MNRAS, 414, 2139
Drake, A., Garel, T., Hashimoto, T., et al. 2017a, A&A, 608, A6 (MUSE UDF SI, Paper VI)
Drake, A. B., Guiderdoni, B., Blaizot, J., et al. 2017b, MNRAS, 471, 267
Dunlop, J. S., McLure, R. J., Robertson, B. E., et al. 2012, MNRAS, 420, 901
Duval, F., Schaerer, D., Östlin, G., & Laursen, P. 2014, A&A, 562, A52
Ellis, R. S., McLure, R. J., Dunlop, J. S., et al. 2013, ApJ, 763, L7
Erb, D. K., Steidel, C. C., Trainor, R. F., et al. 2014, ApJ, 795, 33
Fardal, M. A., Katz, N., Gardner, J. P., et al. 2001, ApJ, 562, 605
Faucher-Giguère, C.-A., Kereš, D., Dijkstra, M., Hernquist, L., & Zaldarriaga, M. 2010, ApJ, 725, 633
Finkelstein, S. L., Papovich, C., Salmon, B., et al. 2012, ApJ, 756, 164
Finkelstein, S. L., Papovich, C., Dickinson, M., et al. 2013, Nature, 502, 524
Forero-Romero, J. E., & Dijkstra, M. 2013, MNRAS, 428, 2163
Furusawa, H., Kashikawa, N., Kobayashi, M. A. R., et al. 2016, ApJ, 822, 46
Garel, T., Blaizot, J., Guiderdoni, B., et al. 2012, MNRAS, 422, 310
Garel, T., Blaizot, J., Guiderdoni, B., et al. 2015, MNRAS, 450, 1279
Garel, T., Guiderdoni, B., & Blaizot, J. 2016, MNRAS, 455, 3436
Gawiser, E., van Dokkum, P. G., Gronwall, C., et al. 2006, ApJ, 642, L13
Grogin, N. A., Kocevski, D. D., Faber, S. M., et al. 2011, ApJS, 197, 35
Gronke, M., & Dijkstra, M. 2014, MNRAS, 444, 1095
Gronke, M., Dijkstra, M., McCourt, M., & Oh, S. P. 2016, ApJ, 833, L26
Gronwall, C., Ciardullo, R., Hickey, T., et al. 2007, ApJ, 667, 79
Guaita, L., Gawiser, E., Padilla, N., et al. 2010, ApJ, 714, 255
Guaita, L., Acquaviva, V., Padilla, N., et al. 2011, ApJ, 733, 114
Haiman, Z. 2002, ApJ, 576, L1
Haiman, Z., Spaans, M., & Quataert, E. 2000, ApJ, 537, L5
Hansen, M., & Oh, S. P. 2006, MNRAS, 367, 979
Hashimoto, T., Ouchi, M., Shimasaku, K., et al. 2013, ApJ, 765, 70
Hashimoto, T., Verhamme, A., Ouchi, M., et al. 2015, ApJ, 812, 157
Hashimoto, T., Ouchi, M., Shimasaku, K., et al. 2017, MNRAS, 465, 1543
Hathi, N. P., Cohen, S. H., Ryan, Jr., R. E., et al. 2013, ApJ, 765, 88

Hathi, N. P., Le Fèvre, O., Ilbert, O., et al. 2016, A&A, 588, A26
Hayes, M., Östlin, G., Schaerer, D., et al. 2013, ApJ, 765, L27
Hayes, M., Östlin, G., Duval, F., et al. 2014, ApJ, 782, 6
Henry, A., Scarlata, C., Martin, C. L., & Erb, D. 2015, ApJ, 809, 19
Herenz, E. C., Gruyters, P., Orlitova, I., et al. 2016, A&A, 587, A78
Herenz, E. C., Urrutia, T., Wisotzki, L., et al. 2017, A&A, 606, A12
Inami, H., Bacon, R., Brinchmann, J., et al. 2017, A&A, 608, A2 (MUSE UDF SI, Paper II)
Inoue, A. K., Shimizu, I., Iwata, I., & Tanaka, M. 2014, MNRAS, 442, 1805
Inoue, A. K., Tamura, Y., Matsuo, H., et al. 2016, Science, 352, 1559
Jiang, L., Egami, E., Fan, X., et al. 2013, ApJ, 773, 153
Kashikawa, N., Shimasaku, K., Matsuda, Y., et al. 2011, ApJ, 734, 119
Kashikawa, N., Nagao, T., Toshikawa, J., et al. 2012, ApJ, 761, 85
Kobayashi, M. A. R., Totani, T., & Nagashima, M. 2010, ApJ, 708, 1119
Koekemoer, A. M., Faber, S. M., Ferguson, H. C., et al. 2011, ApJS, 197, 36
Koekemoer, A. M., Ellis, R. S., McLure, R. J., et al. 2013, ApJS, 209, 3
Konno, A., Ouchi, M., Nakajima, K., et al. 2016, ApJ, 823, 20
Kron, R. G. 1980, ApJS, 43, 305
Kurczynski, P., Gawiser, E., Rafelski, M., et al. 2014, ApJ, 793, L5
Laursen, P., Sommer-Larsen, J., & Razoumov, A. O. 2011, ApJ, 728, 52
Laursen, P., Duval, F., & Östlin, G. 2013, ApJ, 766, 124
Leclercq, F., Bacon, R., Wisotzki, L., et al. 2017, A&A, 608, A8 (MUSE UDF SI, Paper VIII)
Luo, B., Brandt, W. N., Xue, Y. Q., et al. 2017, ApJS, 228, 2
Ma, X., Hopkins, P. F., Faucher-Giguère, C.-A., et al. 2016, MNRAS, 456, 2140
Madau, P. 1995, ApJ, 441, 18
Mainali, R., Kollmeier, J. A., Stark, D. P., et al. 2017, ApJ, 836, L14
Malhotra, S., & Rhoads, J. E. 2002, ApJ, 565, L71
Malhotra, S., Wang, J. X., Rhoads, J. E., Heckman, T. M., & Norman, C. A. 2003, ApJ, 585, L25
Marino, R. A., Cantalupo, S., Lilly, S. J., et al. 2017, ApJ, submitted [arXiv:1709.03522]
Mas-Hesse, J. M., Kunth, D., Tenorio-Tagle, G., et al. 2003, ApJ, 598, 858
Mas-Ribas, L., Dijkstra, M., & Forero-Romero, J. E. 2016, ApJ, 833, 65
Mas-Ribas, L., Dijkstra, M., Hennawi, J. F., et al. 2017, ApJ, 841, 19
Matthee, J., Sobral, D., Darvish, B., et al. 2017, MNRAS, 472, 772
Mawatari, K., Yamada, T., Nakamura, Y., Hayashino, T., & Matsuda, Y. 2012, ApJ, 759, 133
Meurer, G. R., Heckman, T. M., & Calzetti, D. 1999, ApJ, 521, 64
Momose, R., Ouchi, M., Nakajima, K., et al. 2014, MNRAS, 442, 110
Neufeld, D. A. 1991, ApJ, 370, L85
Nilsson, K. K., Möller-Nilsson, O., Møller, P., Fynbo, J. P. U., & Shapley, A. E. 2009, MNRAS, 400, 232
Oesch, P. A., Bouwens, R. J., Carollo, C. M., et al. 2010, ApJ, 709, L21
Oke, J. B., & Gunn, J. E. 1983, ApJ, 266, 713
Ono, Y., Ouchi, M., Shimasaku, K., et al. 2010, ApJ, 724, 1524
Orsi, A., Lacey, C. G., & Baugh, C. M. 2012, MNRAS, 425, 87
Ota, K., Iye, M., Kashikawa, N., et al. 2017, ApJ, 844, 85
Otí-Floranes, H., Mas-Hesse, J. M., Jiménez-Bailón, E., et al. 2012, A&A, 546, A65
Ouchi, M., Shimasaku, K., Akiyama, M., et al. 2008, ApJS, 176, 301
Ouchi, M., Shimasaku, K., Furusawa, H., et al. 2010, ApJ, 723, 869
Oyarzún, G. A., Blanc, G. A., González, V., et al. 2016, ApJ, 821, L14
Oyarzún, G. A., Blanc, G. A., González, V., Mateo, M., & Bailey, III, J. I. 2017, ApJ, 843, 133
Patrício, V., Richard, J., Verhamme, A., et al. 2016, MNRAS, 456, 4191
Rafelski, M., Teplitz, H. I., Gardner, J. P., et al. 2015, AJ, 150, 31
Raiter, A., Schaerer, D., & Fosbury, R. A. E. 2010, A&A, 523, A64
Rakic, O., Schaye, J., Steidel, C. C., & Rudie, G. C. 2011, MNRAS, 414, 3265
Rakic, O., Schaye, J., Steidel, C. C., & Rudie, G. C. 2012, ApJ, 751, 94
Rauch, M., Haehnelt, M., Bunker, A., et al. 2008, ApJ, 681, 856
Rhoads, J. E., Malhotra, S., Dey, A., et al. 2000, ApJ, 545, L85
Rogers, A. B., McLure, R. J., Dunlop, J. S., et al. 2014, MNRAS, 440, 3714
Rosdahl, J., & Blaizot, J. 2012, MNRAS, 423, 344
Salpeter, E. E. 1955, ApJ, 121, 161
Santos, M. R. 2004, MNRAS, 349, 1137
Schaerer, D. 2003, A&A, 397, 527
Schenker, M. A., Ellis, R. S., Konidaris, N. P., & Stark, D. P. 2014, ApJ, 795, 20
Schmidt, K. B., Huang, K.-H., Treu, T., et al. 2017, ApJ, 839, 17
Shapley, A. E., Steidel, C. C., Pettini, M., & Adelberger, K. L. 2003, ApJ, 588, 65
Shibuya, T., Ouchi, M., Nakajima, K., et al. 2014, ApJ, 788, 74
Shibuya, T., Ouchi, M., Konno, A., et al. 2017, PASJ, submitted [arXiv:1704.08140]
Shimasaku, K., Kashikawa, N., Doi, M., et al. 2006, PASJ, 58, 313
Shimizu, I., Yoshida, N., & Okamoto, T. 2011, MNRAS, 418, 2273
Sobral, D., Matthee, J., Darvish, B., et al. 2015, ApJ, 808, 139
Sobral, D., Matthee, J., Best, P., et al. 2017, MNRAS, 466, 1242
Sparre, M., Hayward, C. C., Feldmann, R., et al. 2017, MNRAS, 466, 88
Stark, D. P., Ellis, R. S., Chiu, K., Ouchi, M., & Bunker, A. 2010, MNRAS, 408, 1628
Stark, D. P., Walth, G., Charlot, S., et al. 2015, MNRAS, 454, 1393
Stark, D. P., Ellis, R. S., Charlot, S., et al. 2017, MNRAS, 464, 469
Steidel, C. C., Adelberger, K. L., Giavalisco, M., Dickinson, M., & Pettini, M. 1999, ApJ, 519, 1
Steidel, C. C., Erb, D. K., Shapley, A. E., et al. 2010, ApJ, 717, 289
Steidel, C. C., Bogosavljević, M., Shapley, A. E., et al. 2011, ApJ, 736, 160
Taniguchi, Y., & Shioya, Y. 2000, ApJ, 532, L13
Taylor, P., & Kobayashi, C. 2016, MNRAS, 463, 2465
Trainor, R., & Steidel, C. C. 2013, ApJ, 775, L3
Trainor, R. F., Steidel, C. C., Strom, A. L., & Rudie, G. C. 2015, ApJ, 809, 89
Turner, M. L., Schaye, J., Steidel, C. C., Rudie, G. C., & Strom, A. L. 2014, MNRAS, 445, 794
Verhamme, A., Schaerer, D., & Maselli, A. 2006, A&A, 460, 397
Verhamme, A., Dubois, Y., Blaizot, J., et al. 2012, A&A, 546, A111
Wilkins, S. M., Bunker, A. J., Stanway, E., Lorenzoni, S., & Caruana, J. 2011, MNRAS, 417, 717
Wisotzki, L., Bacon, R., Blaizot, J., et al. 2016, A&A, 587, A98
Yajima, H., Li, Y., Zhu, Q., et al. 2012, ApJ, 754, 118
Zheng, Z., & Wallace, J. 2014, ApJ, 794, 116
Zheng, Z.-Y., Wang, J.-X., Malhotra, S., et al. 2014, MNRAS, 439, 1101
Zitrin, A., Labbé, I., Belli, S., et al. 2015, ApJ, 810, L12

Appendix A: Summary of the public HST data

Table A.1. Summary of the public HST data.

Instrument/ camera	Filter	Effective[a] wavelengths (Å)	2σ[b] depth (AB mag)	5σ[b] depth (AB mag)	Area (arcmin^2)
ACS/WFC3	*F775W*	7693	30.5	29.5	11.4[e]
ACS/WFC3	*F850LP*	9055	29.9	28.9	11.4[e]
WFC3/IR[c]	*F105W*	10 550	31.1	30.1	4.6
[d]			29.7	28.7	6.8[f]
WFC3/IR[c]	*F125W*	12 486	30.7	29.7	4.6
[d]			29.6	28.6	6.8[f]
WFC3/IR[c]	*F140W*	13 923	30.8	29.8	4.6
WFC3/IR[c]	*F160W*	15 370	30.2	29.2	4.6
[d]			29.2	28.2	6.8[f]

Notes. Values taken from Rafelski et al. (2015). [(a)] Effective wavelength. [(b)] Limiting 2 and 5σ magnitudes estimated in an aperture radius of 0.″2. [(c)] Deep and narrow IR data from UDF09 and UDF12 surveys (Oesch et al. 2010; Bouwens et al. 2011; Koekemoer et al. 2013; Ellis et al. 2013). [(d)] Shallow and wide IR data from CANDELS (Grogin et al. 2011; Koekemoer et al. 2011). [(e)] Source catalog in Rafelski et al. (2015) is trimmed to central 11.4 arcmin^2 from the original coverage of 12.8 arcmin^2 (see table comments in Table 1 in Rafelski et al. 2015). [(f)] Source catalog in Rafelski et al. (2015) is trimmed to 4.6 arcmin^2 from the original coverage of 6.8 arcmin^2.